Monthly Notices of the ROYAL ASTRONOMICAL SOCIETY

MNRAS **517,** 526–542 (2022) https://doi.org/10.1093/mnras/stac2676
Advance Access publication 2022 September 22

On large-scale dynamos with stable stratification and the application to stellar radiative zones

V. Skoutnev,[1]★ J. Squire[2] and A. Bhattacharjee[1]

[1]*Department of Astrophysical Sciences and Max Planck Princeton Center, Princeton University, Princeton, NJ 08544, USA*
[2]*Physics Department, University of Otago, Dunedin 9010, New Zealand*

Accepted 2022 September 15. Received 2022 September 15; in original form 2022 August 25

ABSTRACT

Our understanding of large-scale magnetic fields in stellar radiative zones remains fragmented and incomplete. Such magnetic fields, which must be produced by some form of dynamo mechanism, are thought to dominate angular-momentum transport, making them crucial to stellar evolution. A major difficulty is the effect of stable stratification, which generally suppresses dynamo action. We explore the effects of stable stratification on mean-field dynamo theory with a particular focus on a non-helical large-scale dynamo (LSD) mechanism known as the magnetic shear-current effect. We find that the mechanism is robust to increasing stable stratification as long as the original requirements for its operation are met: a source of shear and non-helical magnetic fluctuations (e.g. from a small-scale dynamo). Both are plausibly sourced in the presence of differential rotation. Our idealized direct numerical simulations, supported by mean-field theory, demonstrate the generation of near equipartition large-scale toroidal fields. Additionally, a scan over magnetic Reynolds number shows no change in the growth or saturation of the LSD, providing good numerical evidence of a dynamo mechanism resilient to catastrophic quenching, which has been an issue for helical dynamos. These properties – the absence of catastrophic quenching and robustness to stable stratification – make the mechanism a plausible candidate for generating *in situ* large-scale magnetic fields in stellar radiative zones.

Key words: dynamo – MHD – stars: interiors.

1 INTRODUCTION

Massive stars are born rapidly rotating and quantifying their spin-down throughout the course of stellar evolution is a key issue in stellar astrophysics. The angular momentum present in the radiative interior at the end of a massive star's life has a strong impact on the dynamics of core-collapse and the spin distribution at formation of the subsequent compact remnant (MacFadyen & Woosley 1999; Heger, Langer & Woosley 2000; Yoon, Langer & Norman 2006). Measurements of core rotation rates of red giant stars (Cantiello et al. 2014; Eggenberger et al. 2017; Ouazzani et al. 2019), white dwarf spins (Hermes et al. 2017), rotation periods of neutron stars at birth (Faucher-Giguere & Kaspi 2006; Gullón et al. 2014), and black hole spins by LIGO and Virgo Collaborations (Zaldarriaga, Kushnir & Kollmeier 2018; Roulet et al. 2021) all indicate efficient angular momentum transport in the progenitor cores that cannot be explained generally by hydrodynamic processes. Instead, torques from large-scale magnetic fields generated by a dynamo are often invoked as the dominant form of angular momentum transport in regions of radial differential rotation (DR). The leading candidate is the Tayler–Spruit (TS) dynamo (Spruit 2002), whose recently updated prescription in 1D stellar evolution codes (Fuller, Piro & Jermyn 2019) finds generally improved agreement with observations (Fuller & Lu 2022), although discrepancies remain (Eggenberger et al. 2019; Den Hartogh, Eggenberger & Deheuvels 2020). First-principles investigations of the TS dynamo are pressingly needed to inform 1D prescriptions, similar to the feedback between mixing-length theory and 3D convection simulations in the modelling of stellar convection zones. In particular, we still lack understanding of what non-linear dynamo mechanisms could enable the TS mechanism, remaining viable in the high magnetic Reynolds number and stably stratified conditions of a radiative zone (RZ).

In the global context, the TS dynamo provides torques through the Maxwell stress of axisymmetric poloidal and toroidal magnetic fields whose energy is sourced from the radial DR itself. Successful operation requires closure of a dynamo loop: the axisymmetric toroidal field needs to be generated from the axisymmetric poloidal field and vice versa. The first direction is straightforward and uncontroversial: the toroidal field is generated by winding of the axisymmetric poloidal field by the radial DR. However, the regeneration of the axisymmetric poloidal field remains an open question and is likely a non-linear dynamo effect (Zahn, Brun & Mathis 2007; Fuller et al. 2019). The original Spruit (2002) study suggested that the amplified toroidal field goes unstable to the Tayler instability (Markey & Tayler 1973; Tayler 1973) and creates poloidal field, but as first pointed out by Zahn et al. (2007), this is insufficient because only non-axisymmetric modes are generated by the Tayler instability. Alternatively, follow-up studies proposed that a non-linear dynamo effect such as the α-effect (driven by the helical part of the turbulence from the Tayler instability) may close the dynamo loop (Zahn et al. 2007; Fuller et al. 2019). However, the alpha effect seems to suffer catastrophic quenching at high magnetic Reynolds numbers in the presence of small-scale magnetic fields, which means that the

★ E-mail: valentinskoutnev@gmail.com

© 2022 The Author(s)
Published by Oxford University Press on behalf of Royal Astronomical Society

Downloaded from https://academic.oup.com/mnras/article/517/1/526/6711698 by Princeton University user on 30 August 2023

large-scale dynamo (LSD) might saturate on resistive time-scales [Cattaneo & Hughes 1996; Brandenburg 2001; Rincon 2019; see Brandenburg (2018) and references within on possible ways to avoid quenching]. The time-scales of resistive diffusion can be comparable to or longer than stellar lifetimes. An alternative dynamo mechanism that is immune to quenching and can generate equipartition large-scale magnetic fields on dynamical time-scales is thus desirable.

Such a non-linear dynamo mechanism must also be able to operate in the stably stratified conditions characteristic of stellar RZs. Stable stratification generally tends to suppress dynamo action because it imposes a particular form of anisotropy on the velocity field: fluid motions are unrestricted horizontally while vertical motions are rapidly restored (Riley & Lelong 2000; Billant & Chomaz 2001; Lindborg 2006; Brethouwer et al. 2007; Chini et al. 2022). In the limit of arbitrarily strong stable stratification, the velocity field is approximated by a two-component and three-dimensional field, which is well known to inhibit dynamo action (Zeldovich & Ruzmaikin 1980). Thus, stable stratification and DR tend to play opposite roles in suppressing and supporting dynamo action. Finding a successful dynamo loop driven by DR while surviving the extreme stable stratification of RZs is a primary challenge of stellar interior physics.

One promising mechanism is the magnetic shear-current (MSC) effect, in which large-scale magnetic fields result from the combination of mean shear and non-helical magnetic fluctuations (Rogachevskii & Kleeorin 2004; Squire & Bhattacharjee 2015c, a, 2016). Originally applied in the context of accretion discs, the MSC effect helps explain large-scale magnetic field generation in magnetic turbulence driven by the magnetorotational instability in a sheared (Keplerian) flow (Lesur & Ogilvie 2008; Squire & Bhattacharjee 2015b; Shi, Stone & Huang 2016). In the stellar context, we propose that the MSC effect would operate as follows: a radial shear generates a toroidal field from the poloidal field, whereupon statistical correlations in the non-helical magnetic turbulence lead to an off-diagonal turbulent resistivity that sources poloidal field from the toroidal field, thus closing the dynamo loop. The magnetic fluctuations can in principle originate from a variety of sources including magnetic turbulence from the Tayler instability (Zahn et al. 2007; Fuller et al. 2019) or from a small-scale dynamo (SSD) operating in stably stratified turbulence (Skoutnev, Squire & Bhattacharjee 2021) driven by hydrodynamic instabilities, such as horizontal shear instabilities of latitudinal DR (Zahn 1974, 1992; Prat & Lignières 2013, 2014; Cope, Garaud & Caulfield 2020; Garaud 2020, 2021). Additionally, because the MSC effect is driven by the non-helical part of the magnetic turbulence, the generated large-scale fields are also non-helical and are not subject to magnetohydrodynamic (MHD) helicity constraints.[1] These constraints can lead to so-called catastrophic quenching, whereby LSD saturation occurs at an amplitude, or on a time-scale, that prohibitively scales with the microscopic diffusion coefficients (Gruzinov & Diamond 1994; Bhattacharjee & Yuan 1995; Rogachevskii & Kleeorin 2004; Rincon 2019). An extremely inefficient LSD results in the astrophysical limit of large Rm unless helicity fluxes through the boundaries of the system are sufficiently large (Blackman & Field 2000; Vishniac & Cho 2001; Kleeorin et al. 2000; Brandenburg, Dobler & Subramanian 2002). Because of their non-helical nature, MSC-driven dynamos are unlikely to be affected by catastrophic quenching in the same way as α dynamos driven by helical turbulence. This property, in combination with ample sources of magnetic turbulence and shear flows, make the MSC effect a promising mechanism for locally generating large-scale magnetic fields without restrictions imposed by the level of helicity fluxes in differentially rotating stellar RZs (Kissin & Thompson 2018).

The aim of this paper is to extend mean-field theory to include the effects of stable stratification and subsequently assess the viability of the MSC effect as a dynamo mechanism. This is an important step for a better understanding of large-scale magnetic field generation in the stellar context. The primary issue is the generally unknown effect of stable stratification on LSD mechanisms, particularly in the extreme parameter regimes of high magnetic Reynolds number and strong stable stratification. Can the LSD operate in the background of weak stable stratification? What level of stratification is needed to shut down an LSD mechanism? Where in parameter space are stellar RZs relative to this threshold? We attempt to answer these questions with combined analytical and numerical approaches. We use an available analytical framework (mean-field theory) to study perturbatively the effects of weak stratification on LSDs followed by direct numerical simulations (DNSs) to additionally study the non-perturbative limit of strong stratification. A general agreement between analytic and numerical results allows us to extrapolate these results to realistic parameters for stellar RZs.

1.1 Paper outline

Section 2 presents our local model of a stellar RZ and a mean-field theory framework for the MHD Boussinesq system. This allows perturbative calculation of the modifications to the MSC effect that result from stratification. However, the non-perturbative limit of strong stable stratification relevant to stars lies outside the formally valid regime of mean-field theory and therefore requires numerical exploration. Section 3 then presents sets of DNS, where the effect of varying the stable stratification on the LSD is examined. Section 4 discusses two possible applications of the MSC effect in RZs and Section 5 concludes.

2 THEORETICAL CONSIDERATIONS

2.1 Model of turbulence in an RZ

To most simply capture the physics of a local section of a differentially rotating RZ, we consider a shearing box model as shown in Fig. 1 with an imposed vertical shear profile, stable stratification, and a turbulent velocity field driven with a body force at intermediate scales. The vertical (radial) shear profile represents a local section of radial DR, $\Omega(r)$, which has a shear rate $S = r(\partial\Omega/\partial r)$ in the rotating frame. The driven turbulence represents stably stratified turbulence that may be sourced from an instability. We ignore mean rotation to focus on understanding the novel effect of stable stratification on the LSD, a critical step to the full problem. We discuss the possible effects of mean rotation in Section 4.

This set-up allows a study of the SSD and the LSD as well as their crucial non-linear feedback. We require that (1) the scale separation between the outer box scale and the intermediate forcing scale is large enough to allow an unambiguous definition of large scales and (2) the scale separation between the intermediate forcing scale and the smallest (viscous) scales is large enough to allow a significant turbulent cascade.

The unstratified, non-rotating case of this set-up is actually destabilized by a large-scale hydrodynamic instability known as

[1] Strictly speaking, the MSC effect generates purely non-helical fields only for periodic boundary conditions or for fields that vanish sufficiently fast outside a finite domain. Closed boundary conditions could lead to a shear-current effect that generates helicity (Brandenburg & Subramanian 2005a).

Downloaded from https://academic.oup.com/mnras/article/517/1/526/6711698 by Princeton University user on 30 August 2023

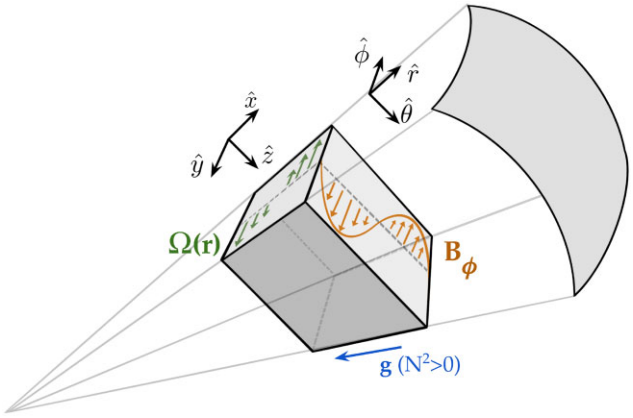

Figure 1. Schematic of a local shearing box embedded in a section of a differentially rotating RZ. Orientation of the Cartesian coordinates used in our set-up are shown relative to the local unit vectors of the spherical coordinate system ($\hat{x} = \hat{r}$, $\hat{y} = -\hat{\phi}$, $\hat{z} = \hat{\theta}$).

the vorticity dynamo (VD; Elperin, Kleeorin & Rogachevskii 2003; Käpylä, Mitra & Brandenburg 2009). The VD generates large-scale vortical (shear) flows and saturates at large amplitudes that may disrupt the operation of an LSD (Teed & Proctor 2016), although it can be suppressed by sufficient rotation (Käpylä, Rheinhardt & Brandenburg 2022). Therefore, it is important to understand the complications caused by the VD. We work through the mean-field framework for both the LSD and VD in the next sections. It will turn out that the VD is also strongly suppressed by stable stratification and so does not play a role in the stratified problem.

2.2 Equations

The standard hydrodynamical model of a stably stratified, collisional plasma with subsonic velocity fluctuations on vertical length scales that are small compared to the local scale-height is the set of Spiegel–Veronis–Boussinesq equations (Spiegel & Veronis 1960). With magnetic fields included, we will call them the MHD Boussinesq equations. In the following sections, we apply the mean-field approach to the MHD Boussinesq equations for the total fields to separate the evolution of the large- and small-scale fields. This allows for an analysis of the two large-scale instabilities of the system: the hydrodynamic VD of the velocity field and the LSD of the magnetic field.

The equations for the total quantities (the velocity field $\boldsymbol{U}_T$, magnetic field $\boldsymbol{B}_T$, buoyancy Θ_T, and pressure P_T) are as follows:

$$\partial_t \boldsymbol{U}_T + \mathbf{U}_T \cdot \nabla \boldsymbol{U}_T = -\nabla P_T + \Theta_T \hat{x} + \boldsymbol{J}_T \times \boldsymbol{B}_T + \nu \nabla^2 \boldsymbol{U}_T + \sigma_f,$$

$$\partial_t \boldsymbol{B}_T = \nabla \times (\boldsymbol{U}_T \times \mathbf{B}_T) + \eta \nabla^2 \boldsymbol{B}_T, \tag{1}$$

$$\partial_t \Theta_T + \boldsymbol{U}_T \cdot \nabla \Theta_T = -N^2 \boldsymbol{U}_T \cdot \hat{x} + \kappa \nabla^2 \Theta_T, \tag{2}$$

$$\nabla \cdot \boldsymbol{U}_T = 0, \ \nabla \cdot \boldsymbol{B}_T = 0, \tag{3}$$

where ν is the kinematic viscosity, η is the resistivity, κ is the thermal diffusivity, σ_f is non-helical forcing at small scales, and $\boldsymbol{B}_T$ is normalized by $\sqrt{4\pi\rho_0}$ (ρ_0 is the constant background plasma density). Note that the 'vertical' direction is aligned with $\hat{x}$. In this formulation (Spiegel & Veronis 1960; Kundu & Cohen 2002; Garaud 2021), the buoyancy field is related to the temperature fluctuations by $\Theta_T = \alpha_V g T_T'$ and the Brunt–Vaisala frequency is given by $N^2 = \alpha_V g(T_{0,x} - T_{\mathrm{ad},x}) > 0$, where $g > 0$ is the local gravitational acceleration, α_V is the coefficient of thermal expansion, and $T_{0,x}$ and $T_{\mathrm{ad},x}$ are the background and adiabatic temperature gradients, respectively.

The mean-field approach splits the total fields into mean and fluctuating components, which we will denote with upper and lower case letters, respectively. We define the mean field as a spatial average over x and y (azimuthal and radial average) of the total field [e.g. $\langle \boldsymbol{B}_T \rangle = \int\int \boldsymbol{B}_T \mathrm{d}x\mathrm{d}y = \boldsymbol{B}(z)$]. Thus, the magnetic field is $\boldsymbol{B}_T = \boldsymbol{B} + \boldsymbol{b}$, the velocity field is $\boldsymbol{U}_T = \boldsymbol{U}' + \boldsymbol{u}$ with $\boldsymbol{U}' = \boldsymbol{U}_0 + \boldsymbol{U}$, and the buoyancy field is $\Theta_T = \Theta + \theta$. Note that the divergence-free conditions require $B_z(z)$ and $U_z(z)$ to be constants (which we set to 0), so the mean magnetic field, for example, is of the form $\boldsymbol{B}(z, t) = (B_x(z, t), B_y(z, t), 0)$. The local radial DR is modelled as an imposed linear shear flow $\mathbf{U}_0 = -Sx\hat{y}$, which varies vertically and flows in the 'toroidal' $\hat{y}$ direction. See Fig. 1 for the geometry. Lastly, to aid with studying the VD, we define the vorticity $\boldsymbol{W}_T = \nabla \times \boldsymbol{U}_T = \boldsymbol{W}' + \boldsymbol{w}$, where $\boldsymbol{W}' = \boldsymbol{W}_0 + \boldsymbol{W}$ and $\boldsymbol{W}_0 = \nabla \times \boldsymbol{U}_0 = -S\hat{z}$.

The mean-field equations are obtained by substituting the scale-separated fields into the equations for the total quantities and taking spatial averages:

$$\partial_t \boldsymbol{W} = \nabla \times \left(\boldsymbol{U}' \times \boldsymbol{W}' + \boldsymbol{J} \times \boldsymbol{B} \right) + \partial_z \Theta \hat{y} + \nabla \times (\nabla \cdot (\langle -\boldsymbol{u}\boldsymbol{u} + \boldsymbol{b}\boldsymbol{b} \rangle)) + \nu \nabla^2 \boldsymbol{W}, \tag{4}$$

$$\partial_t \boldsymbol{B} = \nabla \times (\boldsymbol{U}' \times \boldsymbol{B} + \langle \boldsymbol{u} \times \boldsymbol{b} \rangle) + \eta \nabla^2 \boldsymbol{B}, \tag{5}$$

$$\partial_t \Theta + \boldsymbol{U}' \cdot \nabla \Theta + \langle \boldsymbol{u} \cdot \nabla \theta \rangle = -N^2 \boldsymbol{U} \cdot \hat{x} + \kappa \nabla^2 \Theta, \tag{6}$$

$$\nabla \cdot \boldsymbol{U} = 0, \ \nabla \cdot \boldsymbol{B} = 0, \tag{7}$$

In this form, it is clear that the mean vorticity and mean magnetic field can be driven by the Reynolds and Maxwell stresses, $\boldsymbol{\mathcal{T}} = \langle -\boldsymbol{u}\boldsymbol{u} + \boldsymbol{b}\boldsymbol{b} \rangle$, and the electromotive force, $\boldsymbol{\mathcal{E}} = \langle \boldsymbol{u} \times \boldsymbol{b} \rangle$, respectively, of the fluctuating quantities. The equations for the fluctuating quantities are obtained by subtracting the equations for the mean-fields from the those of the total fields. The fluctuation equations are discussed in Appendix A where they are used to compute transport coefficients.

The small scales contain stably stratified turbulence (driven by σ_f) and the SSD. We now discuss their details as well as the dimensionless parameters of the problem before continuing with mean-field theory of the large scales.

2.3 Dimensionless parameters

Suppose the forcing σ_f at length scale $l_f = 2\pi/k_f$ leads to steady-state turbulence with outer-scale velocity fluctuations u_{rms} prior to the growth of any instabilities. The system is then described by five dimensionless parameters: Re, Sh, Fr, Pm, and Pr. The Reynolds number $\mathrm{Re} = u_{\mathrm{rms}}/k_f\nu$ is the ratio of the viscous time-scale to the outer scale eddy turnover time. The shear number $\mathrm{Sh} = Sl_f/u_{\mathrm{rms}}$ captures the ratio of the outer scale eddy turnover time to the shearing time-scale. The Froude number $\mathrm{Fr} = u_{\mathrm{rms}}/Nl_f$ is the ratio of the gravitational restoring time-scale (Brunt–Vaisala period) to the outer scale eddy turnover time. Lastly, the magnetic Prandtl $\mathrm{Pm} = \nu/\eta$ and thermal Prandtl $\mathrm{Pr} = \nu/\kappa$ numbers measure ratios of diffusivity time-scales. We set both to unity $\mathrm{Pm} = \mathrm{Pr} = 1$ for simplicity in our DNS, but will discuss their expected effects based on theory and previous simulations in Section 4.

Downloaded from https://academic.oup.com/mnras/article/517/1/526/6711698 by Princeton University user on 30 August 2023

2.4 Stably stratified hydrodynamic turbulence

The forcing, σ_f, leads to stably stratified turbulence that provides the background, hydrodynamic turbulence in which the SSD, VD, and LSD may grow. We briefly review properties relevant to the dynamo. When the $\mathrm{Pr} = O(1)$, the turbulent cascade in a stably stratified fluid with energy injection $\epsilon \approx u_{\mathrm{rms}}^3 k_f$ at wavenumber k_f and dissipation at viscous wavenumber k_ν contains two inertial ranges, one above and one below the Ozmidov wavenumber $k_O/2\pi = (N^3/\epsilon)^{1/2}$ where the eddy turnover frequency matches the Brunt–Vaisala frequency (Ozmidov 1992; Brethouwer et al. 2007). At larger scales with wavenumbers less than k_O, the velocity field is highly anisotropic due to the restriction of vertical motions by the stable stratification (Riley & Lelong 2000; Riley & Lindborg 2010). The scale separation between k_f and k_O is controlled by the Froude number $k_O = \mathrm{Fr}^{-3/2} k_f$. At smaller scales with wavenumbers greater than k_O, the velocity field is nearly isotropic due to the negligible effect of buoyancy on the fast time-scales of small eddies. The scale separation between k_O and k_ν is set by the buoyancy Reynolds number $k_\nu = Rb^{3/4} k_O$, where $\mathrm{Rb} = \mathrm{ReFr}^2$. Rb has been found to be the primary control parameter of stably stratified turbulence and needs to be larger than one to avoid the viscosity-affected stratified flow regime where the isotropic inertial range disappears (Billant & Chomaz 2001; Waite & Bartello 2004; Lindborg 2006; Brethouwer et al. 2007; Maffioli & Davidson 2016; Chini et al. 2022). DNS of strong stably stratified turbulence thus simultaneously requires $\mathrm{Fr} \ll 1$ and $\mathrm{Rb} \gg 1$, which is computationally challenging (Bartello & Tobias 2013).

2.5 Small-scale dynamo

The SSD typically has a much faster growth rate than either the VD or LSD and generates magnetic fields primarily on length scales smaller than the forcing scale. Here, we briefly review the instability criterion. The SSD will operate if the turbulence is sufficiently vigorous: magnetic stretching will statistically win over magnetic diffusion and lead to amplification of any seed magnetic field to near-equipartition with the turbulent kinetic energy. In isotropic turbulence, the SSD is unstable when Rm is above a critical value $\mathrm{Rm} > \mathrm{Rm^c} = \mathrm{O}(10^2)$. $\mathrm{Rm^c}$ depends on the magnetic Prandtl number $\mathrm{Rm^c} = \mathrm{Rm^c(Pm)}$ and is higher in the low Pm limit applicable to stellar interiors (Iskakov et al. 2007). When unstable, its exponential growth rate scales as $\gamma_{\mathrm{SSD}} \sim u_{\mathrm{rms}} \mathrm{Re}^{1/2}/l_f$ (Rincon 2019). However, in the presence of stable stratification ($\mathrm{Fr} < 1$) with $\mathrm{Pr} = O(1)$, the largest scales in the system are anisotropic and inefficient at contributing to the dynamo, leading to a reduced effective Rm known as the magnetic buoyancy Reynolds number $\mathrm{Rb_m} = \mathrm{RmFr}^2$ (Skoutnev et al. 2021). The new criterion for the SSD to operate becomes $\mathrm{Rb}_m > \mathrm{Rb}_m^c$, where Rb_m^c has a dependence on Pm (Skoutnev et al. 2021) similar to $\mathrm{Rm^c}$ in isotropic turbulence. Thus, strong enough stable stratification ($\mathrm{Fr} \ll 1$) can shut off the SSD even at high magnetic Reynolds numbers $\mathrm{Rm} \gg \mathrm{Rm^c}$. Note that in the low $\mathrm{Pr} \ll 1$ limit relevant to stellar interiors, the dynamo is more efficient since increased thermal diffusion reduces the effects of buoyancy (see Skoutnev (2022) for the modified instability criterion). In this framework, the SSD operates within the fluctuation equations (see Appendix A) and rapidly provides a source of background magnetic fluctuations that interact with the LSD.

2.6 Mean-field theory

At this point, the mean-field and fluctuation equations together are still exact and just as difficult to solve as the original MHD Boussinesq equations. The primary issue is finding a closure for the evolution of the mean vorticity and magnetic fields driven by $\mathcal{T}$ and $\mathcal{E}$, respectively. To work around this issue, we use the second-order correlation approximation (SOCA), which works with linear fluctuation equations by neglecting the problematic third and higher order terms (Brandenburg & Subramanian 2005b; Rädler & Stepanov 2006; Squire & Bhattacharjee 2015a). This approximation enables a closed system of equations for the mean-field evolution. A background of isotropic small-scale turbulence in both the velocity and magnetic field is assumed on to which anisotropic effects such as shear and stratification are added perturbatively. Physically, the small-scale magnetic field should arise from the SSD, but its statistics are treated as given for this calculation. Arbitrarily small seeds of the mean-fields may then be linearly unstable.

The choice of horizontal averages leaves the mean-field vorticity and induction equations (e.g. $\boldsymbol{J} \times \boldsymbol{B} = 0, \nabla \times (\boldsymbol{U} \times \boldsymbol{B}) = 0$) uncoupled except through $\mathcal{E}$ and $\mathcal{T}$. We make the standard assumption that $\mathcal{E} = \mathcal{E}(\mathbf{B})$ depends only on the mean magnetic field, which decouples the mean-field induction and vorticity equations and allows the VD and LSD to be analysed independently. While it is possible to have joint mean vorticity–magnetic field instabilities (Blackman & Chou 1997; Courvoisier, Hughes & Proctor 2010), simulations in Section 3 support our no-coupling assumption because we always observe the LSD with no accompanying growth of the VD when the VD is suppressed by stratification.

We note that the drastic nature of the SOCA limits the rigorous validity of any results for the LSD to either low magnetic Reynolds numbers $\mathrm{Rm} \ll 1$ (in the limit of low conductivity $l_f^2/\eta\tau_c \ll 1$) or small Strouhal numbers $\mathrm{St} = u_{\mathrm{rms}}\tau_c/l_f \ll 1$ (in the limit of high conductivity $l_f^2/\eta\tau_c \gg 1$), where τ_c is the turbulence correlation time (Brandenburg & Subramanian 2005b). In realistic astrophysical turbulence, Rm is extremely large and St is typically order unity. Results from the SOCA can, as a consequence, be used at most to suggest what effects may be qualitatively operating at $\mathrm{Rm} \gg 1$ and $\mathrm{St} \sim 1$. The combination of DNS at moderate Rm alongside the results from mean-field theory is therefore important to improve our confidence in understanding the dynamo mechanisms that operate in astrophysical regimes.

2.7 Vorticity dynamo

The imposed shear flow in the unstratified case is unstable to a purely hydrodynamic instability known as the VD. We will show that even a small amount of stable stratification in the direction of the imposed mean shear ($\hat{x}$ in our coordinates) will stabilize the VD. We extend the original formulation of the VD in Elperin et al. (2003) to include stable stratification in the framework of mean-field theory. Evolution equations of the mean vorticity field $\boldsymbol{W}(z, t) = (W_x(z, t), W_y(z, t), 0) = (-\partial_z U_y, \partial_z U_x, 0)$ can be written in the form (dropping magnetic field terms):

$$\partial_t W_x = -S W_y - \nu_{xy} S l_f^2 \partial_z^2 W_x + \nu_t u_{\mathrm{rms}} l_f \partial_z^2 W_x, \tag{8}$$

$$\partial_t W_y = -\nu_{yx} S l_f^2 \partial_z^2 W_x + \partial_z \Theta + \nu_t u_{\mathrm{rms}} l_f \partial_z^2 W_y, \tag{9}$$

$$\partial_t \Theta = -N^2 U_x + \nu_t u_{\mathrm{rms}} l_f \partial_z^2 \Theta, \tag{10}$$

where ν_{xy} and ν_{yx} are the dimensionless off diagonal turbulent viscosities and ν_{t} is the dimensionless diagonal turbulent viscosity. These equations are identical to that of Elperin et al. (2003) except for the addition of stratification. We normalize transport coefficients by their expected scalings so that they are dimensionless. Modes of

Downloaded from https://academic.oup.com/mnras/article/517/1/526/6711698 by Princeton University user on 30 August 2023

the form $e^{ik_z z+\gamma t}$ have a growth rate

$$\gamma_{\rm VD} = \frac{u_{\rm rms}}{l_f}\left(\sqrt{-k_z^2 l_f^2 \nu_{yx}{\rm Sh}^2 - {\rm Fr}^{-2}} - \nu_t k_z^2 l_f^2\right), \tag{11}$$

where we use the standard assumptions that the dimensionless transport coefficients are small and there is enough scale separation ($k^2 l_f^2 |\nu_{xy}| \ll 1$). We see that there are growing solutions for small enough k_z, small enough ${\rm Fr}^{-1}$, and $\nu_{yx} < 0$ [ν_{yx} is negative in the unstratified case (Elperin et al. 2003; Käpylä et al. 2009)]. With the addition of stable stratification, it is clear that even weak stratification reduces or possibly fully stabilizes the growth of the VD since the stratification-related term ${\rm Fr}^{-2}$ in equation (11) is not multiplied by any transport coefficients and $|k_z^2 l_f^2 \nu_{yx}| \ll 1$. Any modifications of the transport coefficients (e.g. ν_{yx} or ν_t) by stratification are therefore unimportant because they only appear as higher order corrections to the growth rate.

For a system of arbitrary length in the z-direction, a growing VD with maximum growth rate

$$\gamma_{\rm VD}^{\rm max} = \frac{u_{\rm rms}}{l_f}\left(-Sh^2\nu_{yx}/4\nu_t - \nu_t Fr^{-2}/Sh^2\nu_{yx}\right), \tag{12}$$

occurs at a wavenumber

$$k_{\rm max}^2 l_f^2 = -{\rm Sh}^2\nu_{yx}/4\nu_t^2 + {\rm Fr}^{-2}/{\rm Sh}^2\nu_{yx}. \tag{13}$$

Instability requires that the stratification be weaker than ${\rm Fr}^{-1} < -{\rm Sh}^2\nu_{yx}/2\nu_t$ or the shear stronger than ${\rm Sh} > \sqrt{-2\nu_t/{\rm Fr}\nu_{yx}} \equiv Sh_{\rm VD}^c$. With the assumption ${\rm Sh} = O(1)$ and again that the dimensionless transport coefficients are small (and typically off diagonal turbulent diffusivity coefficients are smaller than the diagonals ones $|\nu_{yx}| \ll \nu_t$), even a weak stratification ${\rm Fr} \approx O(1)$ can shut off the VD. Note that in a finite system, the unstable modes must be able to fit into the domain and so the critical ${\rm Sh}_{\rm VD}^c$ for instability may instead depend on the lowest available wavenumber.

2.8 Large-scale dynamo

In the presence of the imposed shear ($\boldsymbol{U}_0 = -Sx\hat{y}$) and non-helical magnetic fluctuations, the system is unstable to an LSD due to the MSC effect (Squire & Bhattacharjee 2016). Extending mean-field theory to include stable stratification leads to the evolution equations:

$$\partial_t B_x = -\eta_{yx} S l_f^2 \partial_z^2 B_y + \eta_t u_{\rm rms} l_f \partial_z^2 B_x, \tag{14}$$

$$\partial_t B_y = -S B_x - \eta_{xy} S l_f^2 \partial_z^2 B_x + \eta_t u_{\rm rms} l_f \partial_z^2 B_y. \tag{15}$$

Modes of the form $e^{ik_z z+\gamma t}$ have a growth rate:

$$\gamma_{\rm MSC} = \frac{u_{\rm rms}}{l_f}\left(k_z l_f Sh\sqrt{-\eta_{yx}} - \eta_t k_z^2 l_f^2\right), \tag{16}$$

where we have used the standard assumption that transport coefficients are small and there is enough scale separation ($k_z^2 l_f^2 |\eta_{xy}| \ll 1$). There are growing LSD dynamo solutions when the off-diagonal turbulent resistivity is negative $\eta_{yx} < 0$, which occurs only when magnetic fluctuations are present (Squire & Bhattacharjee 2015a). A positive $\gamma_{\rm MSC} > 0$ requires ${\rm Sh} > k_{\rm sys} l_f \eta_t/\sqrt{-\eta_{yx}} \equiv {\rm Sh}_{\rm MSC}^c$ for the lowest wavenumber $k_{\rm sys}$ that fits into the domain. The maximum growth rate and associated wavenumber are given by

$$\gamma_{\rm MSC}^{\rm max} = -\frac{u_{\rm rms}}{l_f}\frac{{\rm Sh}^2\eta_{yx}}{4\eta_t}, \quad k_{\rm max} l_f = \frac{{\rm Sh}\sqrt{-\eta_{yx}}}{2\eta_t}. \tag{17}$$

These predictions are consistent with our simulations in Section 3.4 where we observe that a dominant mode emerges when the domain length L_z is above a critical value and that there are little to no temporal variations in the phase of the growing LSD mode (since the growth rate is purely real).

Unlike for the VD, the mean-field induction equations (14) and (15) look identical to their unstratified case in Squire & Bhattacharjee (2016) except now the transport coefficients can have additional contributions from the effects of stable stratification. We carry out a calculation of the transport coefficients that incorporates Boussinesq effects into the SOCA framework and report here results relevant to the MSC. Details of the calculation are described in the Appendix A. The calculation is general and we also report the effect of stratification on all other transport coefficients in Appendix A, including those driven by helical turbulence.

We find that out of η_{yx}, η_{xy}, and η_t, only the isotropic turbulent resistivity η_t is modified by stable stratification as indeed must be the case due to the perturbative expansion in shear and stratification. So now $\eta_t = \eta_{t,0} + \eta_{t,N^2}$. The modified coefficient is further split up into contributions from the non-helical velocity and magnetic fluctuations, i.e. $\eta_{t,N^2} = \eta_{t,N^2}^{(u)} + \eta_{t,N^2}^{(b)}$. The result is

$$\eta_{t,N^2}^{(u)} = N^2 \int {\rm d}k{\rm d}\omega \frac{3\tilde{\eta}(\tilde{\nu}\tilde{\kappa} - \omega^2)W_u(k,\omega)}{10(\tilde{\eta}^2+\omega^2)(\tilde{\nu}^2+\omega^2)(\tilde{\kappa}^2+\omega^2)}, \tag{18}$$

$$\eta_{t,N^2}^{(b)} = N^2 \int {\rm d}k{\rm d}\omega \frac{(\tilde{\nu}\tilde{\kappa}^2 - (\tilde{\kappa}+2\tilde{\nu})\omega^2)W_b(k,\omega)}{60(\tilde{\nu}^2+\omega^2)^2(\tilde{\kappa}^2+\omega^2)}, \tag{19}$$

where $\tilde{\nu} = \nu k^2$, $\tilde{\eta} = \eta k^2$, $\tilde{\kappa} = \kappa k^2$. $W_u(k,\omega)$ and $W_b(k,\omega)$ are the statistics of the non-helical background velocity and magnetic fluctuations (with the magnetic component assumed to arise from the SSD). We find that for a standard Gaussian model of the fluctuation statistics (Rädler & Stepanov 2006) both contributions of stable stratification to η_{t,N^2} are positive and that the kinetic term is dominant over the magnetic term (see Appendix A). According to equation (17), mean-field theory predicts that weak stable stratification will slightly weaken the growth rate and push the dominant modes to larger scales (lower $k_{\rm max}$). In other words, unlike the VD, we expect the LSD to be slightly modified but remain unstable in the presence of stable stratification, so long as there are still sufficient small-scale magnetic fluctuations.

We note that the generated large-scale fields are non-helical under reasonable boundary conditions (i.e. the total helicity $\mathcal{H} = \int \boldsymbol{B}\cdot\boldsymbol{A}dV = 0$, where $\boldsymbol{A}$ is the vector potential). Further discussion of catastrophic quenching and helicity, in particular why standard arguments for catastrophic quenching likely do not apply to the MSC mechanism, is given in Appendix B.

2.9 Summary of theoretical predictions

2.9.1 *Summary without stratification*

If we start with a seed magnetic field, and turn on forcing at $t = 0$, then (1) the VD will begin to grow if ${\rm Sh} > {\rm Sh}_{\rm VD}^c$, and (2) the SSD will begin to grow if ${\rm Rm} > {\rm Rm}^c$. Once the SSD saturates such that magnetic fluctuations are in equipartition with velocity fluctuations, then the LSD will begin to grow if $Sh > Sh_{\rm MSC}^c$. Once the mean vorticity and magnetic fields become strong, they can possibly interact with each other through their back reaction on the turbulent flow and its statistics. It turns out in DNS (both in this article at moderate ${\rm Re} \approx 120$ and in Teed & Proctor (2016) at low ${\rm Re} \approx 5$), the zonal shear flow of the VD saturates at amplitudes orders of magnitude larger than the original vertical shear and the driving small-scale turbulence. We interpret this as a destabilization of the model because such a strong zonal flow would likely redistribute its energy in the global context on dynamical time-scales and destroy

Downloaded from https://academic.oup.com/mnras/article/517/1/526/6711698 by Princeton University user on 30 August 2023

the steady vertical shear assumed in the local box model. Thus, we argue it is unphysical to consider the LSD in the context of a local box model in the parameter regimes, where the VD is unstable.

2.9.2 *Summary with stable stratification*

With stable stratification that is sufficiently weak, so $\mathrm{Rb}_m = \mathrm{RmFr}^2 > \mathrm{Rb}_m^c$ and $\mathrm{Fr} \sim 1$, at $t = 0$ we expect at least the SSD to grow. The mean-field model predicts a regime where the VD will be stable ($\mathrm{Sh} < \mathrm{Sh}^c_{\mathrm{VD}}$), but the LSD will continue to operate if $\mathrm{Sh} > \mathrm{Sh}^c_{\mathrm{MSC}}$. This is astrophysically interesting since it allows the *in situ* generation of a mean magnetic field without destabilization of the background hydrodynamic flow. Since stable stratification is only added perturbatively in the SOCA, it cannot predict how the LSD will behave with increasingly stronger stratification (increasing Fr^{-1}). Further increasing the stable stratification will slowly suppress the SSD and also increase η_{t,N^2}. Therefore, one can speculate that the LSD should be at least slowly suppressed. As an upper bound, the LSD will stay active at most until the stable stratification is so strong that $\mathrm{Rb}_m < \mathrm{Rb}_m^c$, which is when the SSD is shut down. However, determining the robustness of the LSD for intermediate stratification requires DNS.

3 NUMERICAL STUDY AND RESULTS

3.1 Numerical set-up

We use SNOOPY (Lesur 2015), a 3D pseudo-spectral code, with low-storage third-order Runge–Kutta time stepping and 3/2 de-aliasing to carry out DNS of the MHD Boussinesq equations. Our default domain has a size $(L_x, L_y, L_z) = L(1, 1, 4)$. Periodic boundary conditions are used in the y- and z-direction and shear periodic boundary conditions in the x-direction to model the imposed shear flow $U_0 = -Sx\hat{y}$. The initial seed magnetic field is random at all scales and extremely weak ($E_b(t = 0) = 10^{-16}$) to allow self-consistent amplification by the SSD, if present. The momentum equation is driven with an isotropic, time-correlated forcing term σ_f and the system is integrated in time (alternative forcing types give similar results). This is our model of a local patch of stably stratified turbulence in a differentially rotating stellar RZ, sketched in Fig. 1. A visualization of a representative simulation is shown in Fig. 2.

The forcing is restricted to a waveband of width π/L centred at $k_f = 5 \cdot 2\pi/L$, and has a correlation time $\tau_c = 0.3$, chosen to satisfy the relation $u_{\mathrm{rms}} \approx 2\pi/(k_f\tau_c)$ at early times. The forcing wavenumber k_f is chosen to allow more than an order of magnitude scale separation from the large scale at which the mean-fields are expected to grow (i.e. a scale separation of $k_f L_z/2\pi = 20$), while still supporting a moderate turbulent cascade of the injected energy to the smallest, viscous scales. This turns out to be the minimum scale separation needed to capture the dominant LSD mode, as discussed in Section 3.4. An explicit viscosity, resistivity, and thermal diffusivity (with $\mathrm{Pm} = Pr = 1$) is used to resolve the diffusive scales in the spectral code.

Signatures of the VD and LSD are most visible in two main diagnostics: (1) the isotropic energy spectra and (2) the time evolution of the energy in the large and small scales. The isotropic energy spectrum is defined in the standard way:

$$E_B(k, t) = \sum_{|\boldsymbol{k}|\in[k-\frac{\pi}{L},k+\frac{\pi}{L}]} \frac{1}{2}|\hat{\boldsymbol{B}}_{\boldsymbol{k}}(t)|^2, \tag{20}$$

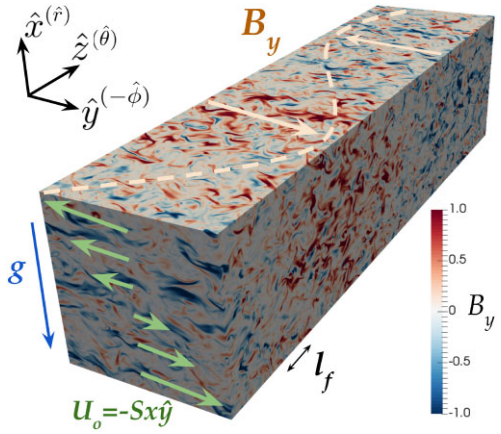

Figure 2. Annotated visualization of the y-component of the magnetic field $B_y(x, y, z)$ from a simulation with $\mathrm{Rm} = 210$, $\mathrm{Sh} = 1$, and $\mathrm{Fr}^{-1} = 3$. Boussinesq stratification (blue arrow) is imposed in the x-direction with Brunt–Väisälä frequency N. A shear flow (green arrows) is imposed in the x-direction with profile $U_0 = -Sx\hat{y}$. Forcing of the momentum equation at length scale $l_f = 2\pi/k_f$ (black arrow) generates velocity fluctuations, which drive an SSD and generates magnetic fluctuations. The subsequent evolution of the large-scale velocity, $U(z)$, and magnetic field, $B(z)$ (light orange), is studied.

where $\hat{\boldsymbol{B}}_{\boldsymbol{k}}(t)$ is the Fourier transform of the magnetic field $\boldsymbol{B}(\boldsymbol{x}, t)$ in the simulation. We define the wavenumber $k_s = 2\pi/L$ as the separation between the large and small scales. Then, the large and small-scale magnetic energies are:

$$E_B(t) = \sum_{k\le k_s} E_B(k, t), \quad E_b(t) = \sum_{k>k_s} E_B(k, t). \tag{21}$$

The analogous definition holds for the kinetic energy spectra, $E_u(k, t)$, and the energy in the large and small-scale velocity fields $E_U(t)$ and $E_u(t)$, respectively. We additionally denote normalized magnetic energy with a tilde, e.g. $\tilde{E}_B(t) = E_B(t)/\overline{E_u(t)}$ where $\overline{E_u(t)}$ is the kinetic energy averaged over the last $50\tau_c$ of a simulation.

3.2 Hydrodynamic VD

3.2.1 *Unstratified VD*

We begin by confirming the results of Elperin et al. (2003) and Käpylä et al. (2009) for the unstratified VD. We increase the shear parameter Sh from $\mathrm{Sh} = 0$ to $\mathrm{Sh} \approx 1$ (by increasing $S = 0$ to $S = 4$) while keeping $\mathrm{Re} \approx 120$ fixed and $\mathrm{Fr}^{-1} = 0$. These runs are hydrodynamic and the diagnostics are shown in grey and blue in Fig. 3. For the energy evolution (top panel), the energy of the mean vorticity field $E_U(t)$ of the high $\mathrm{Sh} \approx 1$ run (solid blue) grows exponentially and saturates at orders of magnitude larger energies than the driven small-scale velocity turbulence, whose baseline level is $E_u(t)$ of the VD-stable runs (dotted grey, green, or orange). The normalized kinetic energy spectra at the last time point (bottom panel) also clearly reveals that the low wavenumber $k < k_s$ modes have more energy than the forcing wave numbers for the VD-unstable simulation (blue), while the same is not true for the run without shear (grey). Additionally, most of the energy in the large-scale modes is dominated by the y-component of the velocity field (not shown). These are the characteristic signatures of the VD that destabilizes this shearing box set-up without stratification.

Downloaded from https://academic.oup.com/mnras/article/517/1/526/6711698 by Princeton University user on 30 August 2023

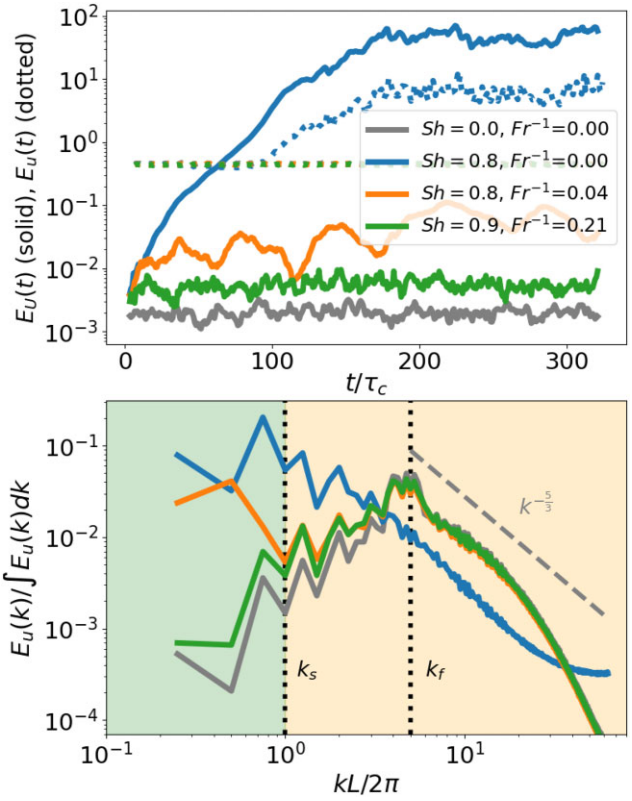

Figure 3. Examination of how the VD is easily stabilized with increasing stratification (increasing Fr^{-1}) along the direction of shear $\hat{x}$. Kinetic energy (top) and spectra (bottom) diagnostics of hydrodynamic simulations with varying shear Sh and stratification Fr^{-1} at fixed Re $\approx$ 120. Solid lines in the top panel are the energy in the mean field, $\mathrm{E_U}$, while dotted lines are the energy in the small-scale velocity field, $\mathrm{E_u}$. The spectra are computed from a snapshot at the last time point. Green and orange shaded regions in the bottom panel represent our definition of the large and small scales. The spectral resolution of the simulations is $N_x \times N_y \times N_z = 192^2 \times 768$ modes.

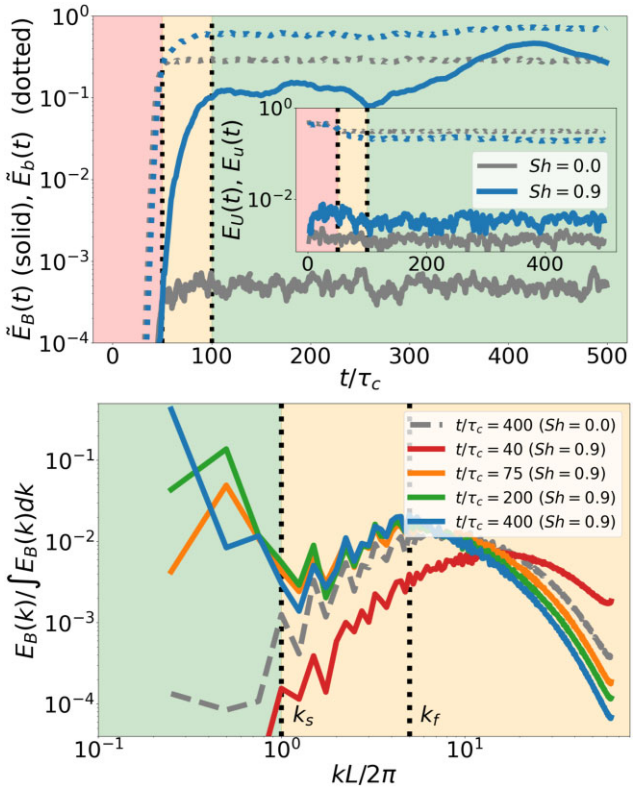

Figure 4. Comparing a simulation with shear (Sh = 0.9) that is unstable to the LSD with a simulation with no shear (Sh = 0). Both simulations have Rm $\approx$ 120, $\mathrm{Fr}^{-1} = 0.2$ with a spectral resolution of $N_x \times N_y \times N_z = 192^2 \times 768$ modes. Top panel: Solid lines are the energy in the mean field normalized by the kinetic energy, $\tilde{E}_B$, while dotted lines are the energy in the small-scale magnetic fields, $\tilde{E}_b$, similarly normalized. The inset plot shows the same diagnostics for the velocity field. Red, orange, and green shaded regions represent the SSD growth phase, LSD growth phase, and the LSD saturated phase. Bottom panel: Normalized magnetic energy spectra at representative times (different colours). Green and orange shaded regions represent our definition of the large and small scales.

3.2.2 Stably stratified VD

To test the mean-field theory prediction, we slowly increase the strength of the background stable stratification and explore the effect on the hydrodynamic VD. We increase the stratification parameter $\mathrm{Fr}^{-1} \in \{0.04, 0.21\}$ while keeping Sh $\approx$ 1 and Re $\approx$ 120 fixed by increasing $N \in \{0.2, 1\}$. Fig. 3 shows the diagnostics in orange and green. Based on the evolution of $E_U(t)$ (top panel), the VD is already only marginally unstable at $\mathrm{Fr}^{-1} = 0.04$ (solid orange) and becomes fully stable at and above $\mathrm{Fr}^{-1} = 0.21$ (solid green). This is also seen in the kinetic energy spectra (bottom panel, orange, and green) where the low wavenumber $k < k_s$ modes remain in subequipartition with the energy at the forcing wavenumber, except in the marginal case (orange) where they are modestly excited. Note that $\mathrm{Fr}^{-1} \geq 1$ corresponds to stratification being important at and above forcing scales (as well as a range of smaller scales), while $\mathrm{Fr}^{-1} < 1$ means stratification only affects scales larger than the forcing scale, which we call weak stratification here. Thus, our simulations qualitatively agree well with the mean-field theory prediction: weak stable stratification easily shuts down the VD. We note that adding magnetic fields to these simulations (not shown) does produce a SSD and LSD (only in the shearing cases), but their addition does not change the above results.

3.3 Stably stratified LSD

3.3.1 Weak stable stratification

We turn to the case of the LSD in turbulence where the stratification is weak, but sufficient to stabilize the VD. The magnetic evolution of a VD stable, weakly stably stratified system proceeds in three main phases as shown in the diagnostics of Fig. 4. A simulation with Rm $\approx$ 120, $\mathrm{Fr}^{-1} = 0.2$, and Sh = 0.9 is compared against one with no shear (Sh = 0) for reference. Both are stable to the VD as shown by the lack of energy growth in the mean velocity field $E_U(t)$ (solid lines of inset plot Fig. 4). The first phase is the kinematic SSD phase (red-shaded region, top panel), characterized by rapid exponential growth of $\tilde{E}_b(t)$ at early times (initially $\tilde{E}_b \approx 10^{-16}$), which ends and begins to saturate around $t/\tau_c \approx 50$ for both cases. Note that in this regime the energy in the mean field $\tilde{E}_B$ also grows at the SSD growth rate due to the contribution of the infrared tail of the SSD eigenfunction in spectral space. After SSD saturation, the growth phase of the MSC effect begins (orange shaded region) and $\tilde{E}_B(t)$ continues to grow at a slower LSD growth rate for the sheared case (solid blue curve, top panel), but completely stops growing for the no shear case (solid grey curve, top panel).

Downloaded from https://academic.oup.com/mnras/article/517/1/526/6711698 by Princeton University user on 30 August 2023

We note that the LSD has a brief pseudo-linear phase from $\tilde{E}_B \approx 5 * 10^{-4}$ to $\tilde{E}_B \approx 5 * 10^{-2}$ where the growth is quasi-exponential, but then transitions to a slower, non-linear growth phase as the LSD begins to saturate. DNS of LSDs driven by magnetic fluctuations can never have a long linear phase because the seed mean-fields inevitably start from moderate amplitudes set by the energy in the infrared wavenumbers of the saturated SSD spectrum. This is a domain-size-dependent effect – if the domain size was increased, the initial seed value of the mean field would decrease and lead to a longer linear phase. However, increasing the domain size any further is currently prohibitively expensive (but see Section 3.4 for a convergence test at a lower Rm).

The majority of the growth phase ends and the LSD saturation phase (green shaded region in top panel) begins for the sheared case around $t/\tau_c = 100$ where the large-scale field energy undergoes a quasi-random behaviour with slow oscillations on the time-scale of hundreds of dynamical times (the origin of the quasi-random oscillations is not understood but is presumably related to the saturation mechanism). The difference compared to the no-shear case is striking as the LSD grows to be nearly in equipartition with the small-scale magnetic fields ($\tilde{E}_B \approx E_b$) around $t/\tau_c \approx 400$. In the no shear case, the random, large-scale fields remain several of orders of magnitude weaker than the small-scale fields ($\tilde{E}_B \ll \tilde{E}_b$) for all times. The difference is also clearly visible in the time evolution of magnetic energy spectra (bottom panel) where the energy in the lowest k modes of the sheared case steadily increases throughout the linear ($t/\tau_c = 75$) and saturation ($t/\tau_c = 200$) phases of the LSD and are nearly four orders of magnitude larger than that of the no shear case (dashed grey) at late times ($t/\tau_c = 400$). Additionally, the lowest-k modes of the sheared case are individually more than an order of magnitude larger in energy than the peak of the magnetic spectra at smaller scales near k_f (this peak is simply that of the saturated SSD). These weakly stratified simulations are in good qualitative agreement with mean-field predictions in limit of perturbative stratification: the VD is easily suppressed while the LSD remains unstable.

3.3.2 *Strong stable stratification*

The next question to address is whether the LSD can operate in stable stratification that is non-perturbative and strong enough to affect the small-scale turbulence ($\mathrm{Fr}^{-1} > 1$). Fig. 5 shows two revealing cases, one where the SSD is strongly suppressed but still active ($\mathrm{Fr}^{-1} \approx 4$, orange) and another where the SSD has been shut down ($\mathrm{Fr}^{-1} \approx 7$, green). The case where the SSD is shut down by strong stratification shows no LSD growth since both $\tilde{E}_b$ and $\tilde{E}_B$ decay, which confirms the expectation that without a source of magnetic fluctuations the MSC effect does not operate. The $\mathrm{Fr}^{-1} \approx 4$ case, however, still shows a robust but slower LSD growth from $t/\tau_c \approx 200$ to $t/\tau_c \approx 600$ when equipartition is reached $\tilde{E}_B \approx \tilde{E}_b$. The low k modes of the magnetic spectra for the $\mathrm{Fr}^{-1} \approx 4$ case (orange, bottom panel) are highly energized. The slower growth rate of the MSC effect is not surprising because the level of magnetic fluctuations is slightly lower due to the strong stratification, which can also been seen by the much lower growth rate of the SSD of the $\mathrm{Fr}^{-1} \approx 4$ case (dashed orange, top panel) compared to the e.g. $\mathrm{Fr}^{-1} = 0.2$ case (dashed blue, top panel). None the less, the final saturation of the LSD is similar in both cases.

Suppression of the dynamo with increasing stratification is quantified in Fig. 6 by showing the equipartition level of the large scale (blue, E_B/E_u) and small-scale (orange, E_b/E_u) magnetic energy at saturation of the LSD (calculated at the end of each simulation)

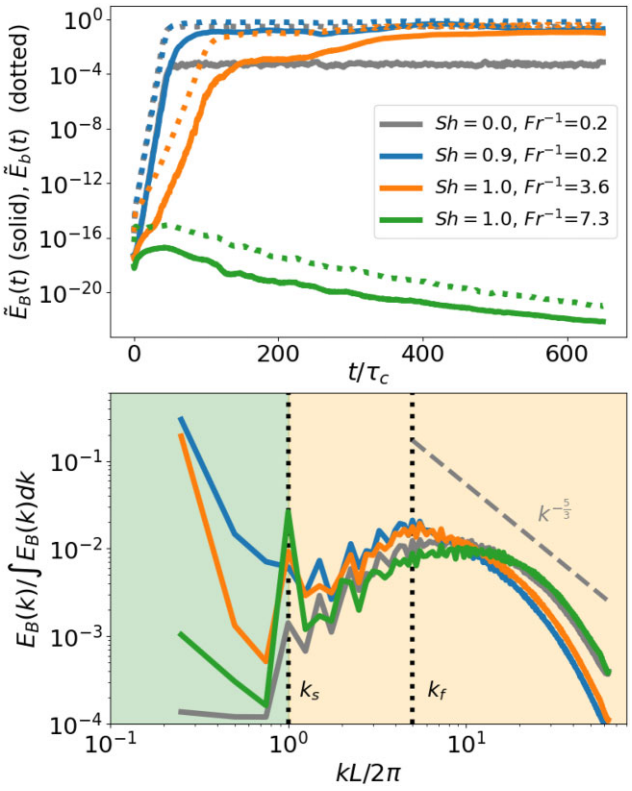

Figure 5. Exploring the effect of stable stratification on the LSD. The LSD appears robust as long as the SSD is unstable. Magnetic energy (top) and spectra (bottom) diagnostics of simulations with increasing stratification (increasing Fr^{-1}) at fixed Rm $\approx$ 120 and Sh $\approx$ 0.9. Solid lines in the top panel are the energy in the mean field, $\tilde{E}_B$, while dotted lines are the energy in the small-scale magnetic fields, $\tilde{E}_b$. The reference simulation with no shear (Sh = 0) is shown in grey. All spectra are computed from a snapshot at the last time point. Green and orange shaded regions in the bottom panel represent our definition of the large and small scales. The spectral resolution of the simulations is $N_x \times N_y \times N_z = 192^2 \times 768$ modes.

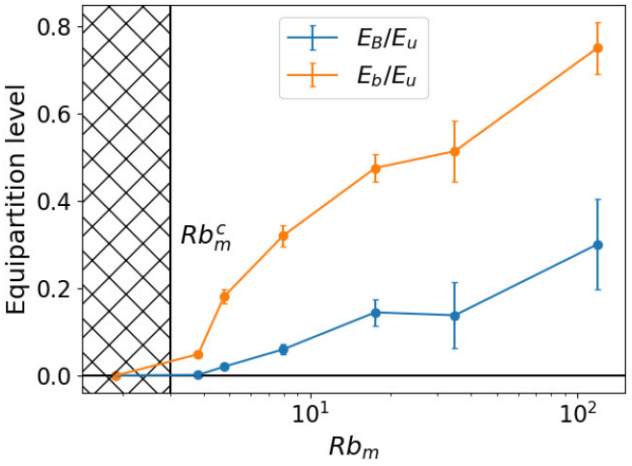

Figure 6. The equipartition level of the saturated magnetic field with varying stratification. Coloured lines show the energy fraction of large-scale (blue) and small-scale (orange) magnetic fields relative to the turbulent kinetic energy as a function of $\mathrm{Rb}_m = \mathrm{RmFr}^2$. The simulations with increasing stratification (decreasing Rb_m) are carried out at constant Rm $\approx$ 120, Sh $\approx$ 1. Energies and standard deviations are calculated long after saturation from the last $50\tau_c$ in each run. Hashed region denotes where the SSD is inactive due to strong stratification (for $\mathrm{Rb}_m < \mathrm{Rb}_m^c = 3$ when Pm = 1).

Downloaded from https://academic.oup.com/mnras/article/517/1/526/6711698 by Princeton University user on 30 August 2023

versus the stratification parameter $\mathrm{Rb}_m = \mathrm{RmFr}^2$. Fig. 6 is generated from a series of simulations that vary Fr at fixed $\mathrm{Rm} \approx 120$ and $\mathrm{Sh} \approx 1$. It appears that the LSD robustly operates in the non-perturbative limit of strong stratification ($\mathrm{Fr}^{-1} > 1$) with a near-equipartition saturation level of $E_B/E_u = O(10^{-1})$. The LSD begins to shut down when the SSD itself is strongly suppressed as Rb_m approaches Rb_m^c from the right.

These idealized numerical results suggest that if an RZ with vertical shear contains stably stratified turbulence with a sufficiently large $\mathrm{Rb}_m > \mathrm{Rb}_m^c$ to sustain the SSD, the MSC should drive a large-scale magnetic field that reaches near-equipartition with the turbulent kinetic energy.

3.4 Role of the incoherent dynamo and aspect ratio

3.4.1 Incoherent dynamo

Finite size domains are susceptible to an additional LSD mechanism known as the incoherent dynamo and its contribution relative to a coherent shear-current effect remains a matter of debate. Studies that have attempted to directly measure η_{yx} for different setups, parameter regimes, and test-field methods report different signs for η_{yx} [see Zhou & Blackman (2021) for a thorough review]. Singh & Sridhar (2011) show that a kinematic shear-current effect cannot operate for any Sh at low $\mathrm{Re} \sim \mathrm{Rm} \lesssim 1$, leaving only the $\mathrm{Rm} \gg 1$ regime as a possibility. Unfortunately, in this regime with full MHD background turbulence at moderate Rm, test-field methods that account for the magnetic background turbulence become only approximate and many variants are possible (Rheinhardt & Brandenburg 2010; Käpylä et al. 2022). Compressible MHD setups with driven turbulence, $\mathrm{Sh} \lesssim 0.5$, $\mathrm{Re} \gtrsim 1$, $\mathrm{Rm} \lesssim 100$, and scale separation $k_f L_z/2\pi \leq 10$, find η_{yx} to be slightly positive or slightly negative but not statistically different than zero in single realizations, concluding that incoherent effects are dominating (Brandenburg et al. 2008; Käpylä et al. 2022). Incompressible MHD simulations with driven turbulence at $\mathrm{Sh} \lesssim 0.5$, $\mathrm{Re} \sim \mathrm{Rm} \lesssim 15$, and $k_f L_z/2\pi = 6$ find a statistically significant negative value of η_{yx} from ensembles of simulations (Squire & Bhattacharjee 2016), but the fitting assumptions used to reduce measurement noise have been debated. To add to the confusion, simulations of MRI-driven MHD turbulence in a finite volume code (Shi et al. 2016) and a moving mesh code (Zier & Springel 2022) have reported negative measurements of η_{yx}, while Wissing et al. (2022) report a positive measurement using a smooth particle hydrodynamics code. Zhou & Blackman (2021) resolve some of these discrepancies (at least at low and moderate Re) by showing that the kinetic contribution $\eta_{yx}^{(u)}$[2] is sensitive to the spectral slope at low wavenumbers and becomes less efficient at counter-acting the generally negative $\eta_{yx}^{(b)}$ at higher Re (i.e. $\eta_{yx}^{(u)}$ becomes less positive or even negative, possibly contributing to the MSC effect at high enough Re).

As an alternative approach in the $\mathrm{Re} = \mathrm{Rm} > 50$ regime of this study, we do an indirect experiment that takes advantage of the volume independence/dependence of coherent/incoherent effects to test their relative contributions. The primary incoherent dynamo in a shear flow and non-helical turbulence is the stochastic-α effect, in which zero-mean fluctuations of the α transport coefficients can drive growth of the variance of the mean-field $\langle \boldsymbol{B}^2 \rangle$ despite a zero ensemble average mean-field $\langle \boldsymbol{B} \rangle = 0$ (Vishniac & Brandenburg 1997; Brandenburg & Subramanian 2005b; Heinemann, McWilliams & Schekochihin 2011; Mitra & Brandenburg 2012). These statistical properties make the stochastic-α effect dependent on the domain size unlike coherent dynamo effects (Squire & Bhattacharjee 2015d).

The scaling of an incoherent dynamo with volume can be determined as follows. For the simplest case, consider zero mean $\langle \alpha_{yy}(t) \rangle = 0$ fluctuations with a variance $\langle \alpha_{yy}(t)\alpha_{yy}(t') \rangle = D_{yy}\delta(t-t')$, which corresponds to a fluctuating EMF of the form $\mathcal{E}_y = \alpha_{yy}(t)B_y$ (Mitra & Brandenburg 2012). One can show that the fastest growing mode has a growth rate that scales as $\gamma_\alpha^{\max} \propto D_{yy}^{1/2}$ (Vishniac & Brandenburg 1997). Because increasing the volume of the domain by a factor of N decreases the variance D_{yy} of the α_{yy} fluctuations by a factor of N (assuming each of the N sub-volumes are statistically independent), the stochastic dynamo growth rate must scale with the inverse square root of the domain volume $\gamma_\alpha^{\max} \propto V^{-1/2}$ (Squire & Bhattacharjee 2015d). Therefore if our simulations are dominated by an incoherent effect, we should expect a significant decrease in the strength of the LSD when the volume is increased.

We carry out this experiment by progressively doubling or quadrupling the volume $V = L_x L_y L_z$ by changing the box aspect ratio $(L_x, L_y, L_z)/L = (1, 1, 4)$, $(1, 1, 8)$, $(2, 2, 4)$, and $(4, 4, 4)$ at fixed turbulent forcing scale and fiducial parameters $\mathrm{Rm} \approx 60$, $\mathrm{Sh} \approx 1.0$, $\mathrm{Fr}^{-1} \approx 0.2$. These parameters are stable to the VD, but unstable to the SSD and LSD. As discussed earlier in Section 3.3, the growth rate of the LSD right after the SSD saturates is difficult to interpret because the pseudo-linear phase of the LSD is short in finite size simulations. To ameliorate this issue, we run an ensemble of simulations for each case to quantify the variance of the LSD evolution instead of relying on comparison between single realizations. The (1, 1, 4), (1, 1, 8), (2, 2, 4), and (4, 4, 4) cases each have 20, 5, 5, and 3 runs in their ensembles, respectively.

The results are shown in Fig. 7 and the measured mean and standard deviation of the growth rate γ_{LSD} of each ensemble are reported in Table 1. If the LSD was driven by an incoherent effect, we would expect the growth rate to decrease by a factor of $\sqrt{2}$, 2, and 4 for the (1, 1, 8), (2, 2, 4), and (4, 4, 4) boxes compared to the (1, 1, 4) box. A strong volume dependence does not appear to be observed. The measured growth rates in Table 1 have a volume dependence $\gamma_{\mathrm{LSD}} \sim V^{-0.23 \pm 0.1}$ that is weaker than the $V^{-0.5}$ that would be theoretically expected if the observed LSD a purely an incoherent effect. The ensemble mean of the (1, 1, 8) and (2, 2, 4) cases in the top plot of Fig. 7 both fall within the ensemble variance of the (1,1,4) runs before beginning their slow, random oscillations in the saturated phase $t/\tau_c \gtrsim 250$. The ensemble mean of the (4, 4, 4) case has a noticeably slower quasi-exponential growth, but this may be due to a lack of statistical convergence since the ensemble is small with size of 3 (constrained by the increased computational cost of the larger domain). The ensemble mean appears to be heavily influenced by a single run whose growth stagnates for $125 \lesssim t/\tau_c \lesssim 200$ but then resumes growing at a comparable rate to the others for $200 \lesssim t/\tau_c \lesssim 250$. At late times, all aspect ratios saturate at similar energies and with similar magnetic spectra as shown in the bottom plot of Fig. 7.

Examining the phase variation of the mean field over time also offers an additional way to check for the presence of incoherence effects. An incoherent effect would generate a mean field with a randomly wandering phase (Squire & Bhattacharjee 2015d), while the dispersion relation of the coherent MSC effect predicts no phase variation since γ^{MSC} is purely real (equation 17). The space–time plots of individual runs in Fig. 8 demonstrate that the mean-field $B_y(z, t)$ maintains a constant phase for many LSD-growth time-scales ($\gamma_{\mathrm{LSD}}^{-1} \sim 20\tau_c$ from Table 1) in the saturation

[2]The transport coefficient can be broken up into contributions from the velocity and magnetic fluctuations: $\eta_{yx} = \eta_{yx}^{(u)} + \eta_{yx}^{(b)}$.

Downloaded from https://academic.oup.com/mnras/article/517/1/526/6711698 by Princeton University user on 30 August 2023

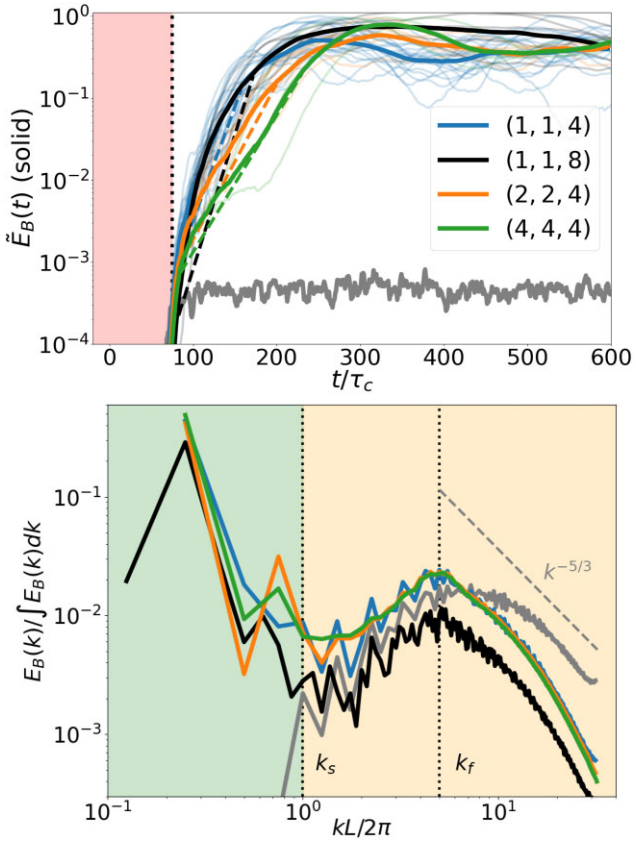

Figure 7. A validation test using ensembles of runs for different domain sizes (L_x, L_y, L_z) shows that incoherent dynamo effects are likely subdominant and that our fiducial domain size (1, 1, 4) is sufficiently large to capture the dominant LSD mode. Top figure shows the evolution of the mean magnetic field energy for each case. Individual runs have low opacity while the run geometrically averaged over the ensemble is shown in full opacity for each aspect ratio. Dashed lines are the exponential fit to the LSD growth phase based on the average of the individually measured growth rates from the ensemble. The red shaded region for $t/\tau_c \lesssim 75$ is the SSD growth phase. Bottom figure shows the magnetic energy spectra obtained at the end of the simulations. All simulations have fixed values of $\mathrm{Rm} \approx 60$, $\mathrm{Sh} \approx 1.0$, and $\mathrm{Fr}^{-1} \approx 0.2$ and the spectral resolution is scaled with the aspect ratio (the fiducial (1, 1, 4) simulation has $N_x \times N_y \times N_z = 96^2 \times 384$ modes). Unlabelled grey curves are the no-shear ($\mathrm{Sh} = 0$) simulation for reference.

Table 1. Mean and standard deviations of the LSD growth rates γ_{LSD} for each ensemble of simulations with different aspect ratios (whose time evolution is shown in Fig. 7). The growth rate for any single realization is measured between the time when the SSD saturates, t_{start}, and when the mean field energy reaches 25 per cent of its maximum value $\widetilde{E}_B(t_{\mathrm{end}}) = 0.25\max(\widetilde{E}_B(t))$. We define SSD saturation by when the SSD growth rate falls below 10 per cent of its maximum value, $\gamma_{\mathrm{SSD}}(t_{\mathrm{start}}) = 0.1\max(\gamma_{\mathrm{SSD}}(t))$ where $\gamma_{\mathrm{SSD}}(t) = \partial_t \ln(E_b(t))$. Note that the size of the ensembles of the larger volume cases are smaller due to computational costs.

Aspect ratio	$\gamma_{\mathrm{LSD}} l_f/u_{\mathrm{rms}}$
(1, 1, 4)	$(6.1 \pm 1.3) \times 10^{-2}$
(1, 1, 8)	$(7.0 \pm 1.5) \times 10^{-2}$
(2, 2, 4)	$(4.1 \pm 0.6) \times 10^{-2}$
(4, 4, 4)	$(3.6 \pm 0.8) \times 10^{-2}$

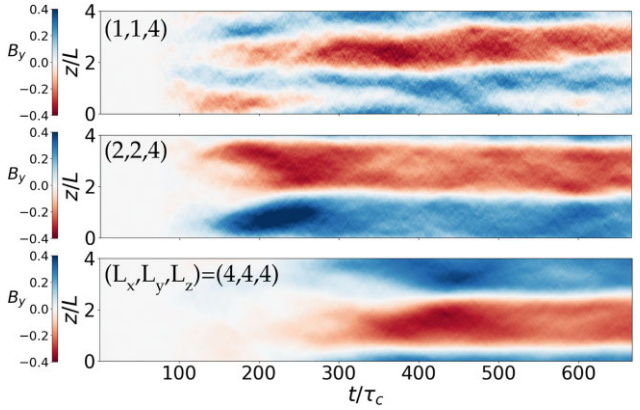

Figure 8. Visual validation that the phase of the saturated LSD mode remains coherent for long times. Time–space plots from single realizations of the y-component of the magnetic field $B_y(z, t) = \langle B_y(x, y, z, t)\rangle_{x,y}$ for three aspect ratios denoted in the top left corner of each plot. The (1, 1, 4) run was carried out further to $t/\tau_c = 1200$ with no qualitative change in behaviour (not shown).

regime $t/\tau_c \gtrsim 300$ and that the mean-field of the larger volume runs appears progressively more coherent and smooth. The (1, 1, 4) and (2, 2, 4) domains are further run until $t/\tau_c = 3000$ (see Appendix C) for a thorough check on the long term behaviour of the saturated LSD. Fig. C1 shows that the (1, 1, 4) case begins to exhibit phase variation for $t/\tau_c > 1000$, suggesting unknown behaviour of the saturated LSD, the presence of an incoherent effect, or interaction of the two. However, the (2,2,4) exhibits no phase variation for the entire duration, which we interpret as the sufficiently large domain size where incoherent effects have become insignificant.

Overall, the weak volume dependence on the LSD growth rate and a fairly coherent constant-phase evolution with time suggests that incoherent effects have a subdominant contribution to the total LSD growth rate in our simulations. A contribution from an incoherent effect [likely strongest in the (1, 1, 4) case] may explain the slight decrease in the LSD growth rate with increased simulation volume at a fixed forcing scale. LSDs in realistic astrophysical systems may be expected to be dominated by either incoherent or coherent effects depending on the scale separation, which is not always asymptotically large.

3.4.2 *Aspect ratio and convergence*

While changing the aspect ratio, we can also check if our simulations are converged in the z-dimension (Yousef et al. 2008). A comparison of the magnetic spectra in the bottom panel of Fig. 7 of the (1, 1, 4) and (1, 1, 8) aspect ratios shows that the MSC effect is fully captured in our (1, 1, 4) runs since the dominant mode is clearly the $kL/2\pi = 1/4$ mode in the larger (1, 1, 8) simulation (black). This qualitatively agrees with the dispersion relation equation (17) which predicts a dominant wavenumber k_{max}. Additionally, the time evolution of $E_B(t)$ of both cases is similar in the growth phase and after they enter the saturation regime $t/\tau_c \gtrsim 250$ and slowly oscillate with similar amplitudes. In summary, we find that a minimum scale separation of $k_f L_z/2\pi = 20$ is needed to capture the LSD at these parameters and that our fiducial (1,1,4) simulations are sufficiently long in the z direction.

Downloaded from https://academic.oup.com/mnras/article/517/1/526/6711698 by Princeton University user on 30 August 2023

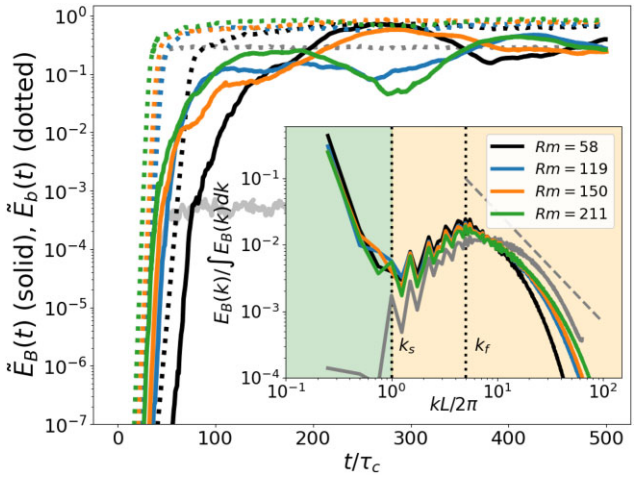

Figure 9. A test demonstrating that the MSC effect is likely free of quenching. Simulations with increasing Rm (at Pm = 1) are carried out by decreasing η while keeping $Sh = 0.9$ and $\mathrm{Fr}^{-1} = 0.2$ fixed. Magnetic energy (main figure) and spectra (inset figure) diagnostics are shown. The large scales of the magnetic spectra and saturation of the LSD appear to be unaffected. Unlabelled grey curves are the no-shear (Sh = 0) simulation for reference. The spectral resolution of the Rm = 58, 119 runs is $N_x \times N_y \times N_z = 192^2 \times 768$ modes and of the Rm = 150, 211 runs is $288^2 \times 1152$.

3.5 Rm dependence of the MSC effect

An outstanding problem in dynamo theory is understanding the amplitude and time-scale of non-linear saturation of various LSD mechanisms in the limit of large Rm, as relevant to the astrophysical regime. LSDs based on the α-effect face the well-known issue of catastrophic quenching, in which the amplitude and/or time-scale of saturation scales strongly with the microscopic resistivity, suggesting an extremely weak LSD in the Rm $\gg$ 1 regime (Brandenburg & Subramanian 2005b; Rincon 2019). Although possibilities such as helicity fluxes through boundaries (Blackman & Field 2000; Kleeorin et al. 2000; Vishniac & Cho 2001; Brandenburg et al. 2002) and alternative scalings of small-scale helicity dissipation (Brandenburg et al. 2002; Brandenburg & Subramanian 2005b; Blackman 2016) may resolve the problem, simulations so far have given mixed results (Brandenburg & Subramanian 2005b; Rincon 2021). Because the MSC effect is non-helical, the usual helicity constraints that cause quenching do not apply (see Appendix B). This means there is no a priori reason that it should be catastrophically quenched, making it a promising mechanism that may operate at astrophysically large Rm.

To test the Rm dependence of the MSC effect, we carry out a Rm scan at Pm = 1 to computationally accessible values, with all other parameters fixed. The fiducial parameters are Sh $\approx$ 1.0 and $\mathrm{Fr}^{-1} \approx$ 0.2 as before. Rm is increased by a factor of four from Rm $\approx$ 50 up to Rm $\approx$ 200 by decreasing η. A sign of catastrophic quenching in this test would be to observe the growth rate or saturation amplitude progressively decrease as a near power law with increasing Rm, as observed in helical dynamo simulations (Bhat, Subramanian & Brandenburg 2016; Rincon 2021). Hence, the factor of 4 difference between the Rm $\approx$ 50 and Rm $\approx$ 200 simulations should have an easily discernible effect. The result is shown in Fig. 9 where we find that the LSD has no systematic *Rm* dependence. Increasing Rm only increases the SSD growth rate, as expected; which is seen through the progressively earlier saturation of $\tilde{E}_b(t)$ (dotted lines). This causes the LSD ($\tilde{E}_B(t)$, solid lines) to begin growth earlier, but they subsequently grow at a similar rate (albeit with the random oscillations discussed earlier) and each run saturates at a similar level. Indeed, these runs at different Rm are not more dissimilar than runs from the ensemble of 20 simulations in Fig. 7 at the same Rm $\approx$ 60 for the (1, 1, 4) case (after SSD saturation). Additionally, the magnetic spectra in the inset panel are independent of Rm at large scales (low k).

Thus our test finds no signs of catastrophic quenching with increasing Rm up to the largest computationally accessible value of Rm $\approx$ 200. These numerical results, in combination with the above theoretical arguments, strongly suggest that the MSC effect is a dynamo mechanism free of catastrophic quenching that may operate in the astrophysicaly large Rm regime applicable to RZs.

4 APPLICATION TO RZS

Our proposal is that the MSC effect may be an important non-linear dynamo mechanism that closes the global dynamo loop in differentially rotating RZs. Axisymmetric toroidal fields may grow from the shearing (from radial DR) of an axisymmetric poloidal if there is a source of non-helical magnetic fluctuations to drive the MSC effect and regenerate the axisymmetric poloidal field, closing the dynamo loop. We discuss two avenues for producing magnetic fluctuations (1) Tayler-instabilities of the toroidal field and (2) SSD operating in stably stratified turbulence driven by horizontal shear instabilities of latitudinal DR. We assume that the MSC effect is agnostic to the instability that sources the magnetic fluctuations and that the turbulence is predominantly non-helical at small scales. We leave studies of specific instabilities for future work.

4.0.1 *Tayler instabilities*

In the framework of the TS dynamo, a sufficiently strong toroidal field is unstable to kink-type modes known as Tayler instabilities (Tayler 1973), leading to magnetic turbulence. The Tayler modes are non-axisymmetric and themselves cannot be directly sheared to regenerate the axisymmetric toroidal field, but instead are argued to contribute to a non-linear dynamo mechanism that regenerates the axisymmetric poloidal field (Zahn et al. 2007; Fuller et al. 2019). The MSC effect is a natural candidate mechanism because it is driven by magnetic fluctuations and is robust to stable stratification as shown in this study. Suggestions of an alpha based mechanism by previous studies (Zahn et al. 2007; Fuller et al. 2019) are complicated by the known issue that small-scale magnetic fields generally suppress the alpha-effect and likely cause catastrophic quenching at the high Rm regime relevant to RZs, as discussed earlier. The Rm-independent nature of the MSC effect makes it a promising alternative.

4.0.2 *Horizontal shear instabilities*

Another pathway way to generate magnetic fluctuations in a RZ is through the SSD operating in stably stratified turbulence driven by hydrodynamic instabilities. A likely possibility is horizontal shear instability of latitudinal DR. Vertical shear instabilities of radial DR, while generally stronger than latitudinal DR (Zahn 1992), are most likely stabilized by the strong stratification in RZs (Garaud 2021). We propose that magnetic fluctuations from the SSD combined with radial DR may generate mean toroidal and poloidal fields through the MSC effect. Extrapolating from the results of Section 3 suggests the toroidal field would reach near-equipartition with the turbulence sourced by instability of the latitudinal DR. Note that our local shearing box set-up cannot capture such instabilities directly,

Downloaded from https://academic.oup.com/mnras/article/517/1/526/6711698 by Princeton University user on 30 August 2023

because we do not include a horizontal shear, but heuristically captures the resulting small-scale turbulence through the external forcing term. Here, we use dimensionless numbers estimated based on helioseismology of the solar tachocline (Hughes, Rosner & Weiss 2007), the upper portion of the solar RZ, to examine the feasibility of our proposal.

The tachocline is approximately a thin spherical shell with radius $R = 0.7\mathrm{R}_\odot$, thickness $\Delta R \approx 10^{-2}R$, and DR profile $\Omega(r, \theta)$. For the latitudinal DR, the differential angular velocity between the equator and the poles $(\Delta\Omega)_\theta$ is approximately $O(10^{-1})$ of the solar rotational frequency, i.e. $(\Delta\Omega)_\theta \approx 0.1\Omega_\odot$. For the radial DR, the differential angular velocity between the top and bottom of the tachocline at the equator is of similar strength $(\Delta\Omega)_r \approx 0.1\Omega_\odot$. Turbulence from the horizontal shear instabilities has an upper bound on the turbulent velocity $u_{\mathrm{rms}} \sim (\Delta\Omega)_\theta R$ and an effective forcing wavenumber likely comparable to $k_f \sim 2\pi/R$ (Cope et al. 2020; Garaud 2020). The radial DR provides mean shear that is stable (Garaud 2021) with a shear frequency that we estimate as $S = r(\partial\Omega/\partial r) \approx R(\Delta\Omega)_r/\Delta R$. The associated dimensionless numbers are

$$\mathrm{Re} = 8 \times 10^{13} \left(\frac{R}{5 \times 10^8\,\mathrm{m}}\right)^2 \left(\frac{\Delta\Omega_\theta}{3 \times 10^{-7}\mathrm{s}^{-1}}\right) \times \left(\frac{\nu}{10^{-3}\,\mathrm{m}^2\,\mathrm{s}^{-1}}\right)^{-1}, \tag{22}$$

$$\mathrm{Fr} = 3 \times 10^{-4} \left(\frac{\Delta\Omega_\theta}{3 \times 10^{-7}\mathrm{s}^{-1}}\right) \left(\frac{N}{10^{-3}\,\mathrm{s}^{-1}}\right)^{-1}, \tag{23}$$

$$\mathrm{Rb}_m = 7 \times 10^4 \left(\frac{\mathrm{Pm}}{10^{-2}}\right) \left(\frac{\mathrm{Re}}{8 \times 10^{13}}\right) \left(\frac{\mathrm{Fr}}{3 \times 10^{-4}}\right)^2, \tag{24}$$

$$Sh = 10^2 \left(\frac{\Delta\Omega_r/\Delta\Omega_\theta}{1}\right) \left(\frac{R/\Delta R}{10^2}\right). \tag{25}$$

Comparing the magnetic buoyancy Reynolds number $\mathrm{Rb}_m = O(10^4)$ to the critical value $\mathrm{Rb}_m^c = O(10)$ suggests that the SSD is unstable (Skoutnev et al. 2021). The combination of a large shear number $Sh \gg 1$ and an SSD providing magnetic fluctuations satisfies two the criteria for operation of the MSC effect. Therefore the MSC effect may generate near-equiparition magnetic fields with $B_\phi = O(1)T$, where we have use the equipartition estimate $B_\phi^2/2\mu_0 \sim \rho u_{\mathrm{rms}}^2/2$ with $\rho \approx 200$ kg m^{-3}. We expect these scalings to be reasonable in the interior of RZs of stars, where latitudinal DR provides the dominant source of turbulence and the MSC effect is operating in isolation.

4.0.3 *Effect of rotation and low Prandtl numbers*

We briefly describe the possible modifications to our results by additional effects in RZs not explored in our study, that of rotation and low Prandtl numbers. These are likely subdominant to effects of strong radial shear and stable stratification in RZs. Rotation modifies the MSC effect directly through an orientation-dependent contribution to η_{yx} and will have a significant effect if $S/\Omega \lesssim 1$ (Squire & Bhattacharjee 2015d). While this is likely not important in the tachocline where $S/\Omega \approx ((\Delta\Omega)_r/\Omega_\odot)(R/\Delta R) \approx 10$, it may be important in other stars with weaker radial DR or faster rotation. Another important source of uncertainty are the effects of low Prandtl numbers typical of stellar interiors [$\mathrm{Pm} = O(10^{-2})$, $\mathrm{Pr} = O(10^{-6})$ in the tachocline (Garaud 2021)]. A lower Pm generally makes a SSD more difficult to sustain (Iskakov et al. 2007), which is captured by the dependence of $Rb_m^c(Pm)$ on Pm (Skoutnev et al. 2021). However, for the LSD, calculations with the SOCA have found that the MSC effect is not sensitive to Pm (Squire & Bhattacharjee 2015a). Unfortunately, confirming these results for the LSD with DNS at low Pm is currently impractical due to an even larger requirement for Re. On the other hand, a low $Pr = \nu/\kappa$ is expected to make the SSD and therefore the LSD more unstable (Skoutnev 2022). A higher thermal diffusivity, κ, decreases the effect of stratification and leads to more isotropic turbulence, which generally enables more efficient dynamo action.

5 CONCLUSION

We examine the effects of stable stratification on mean-field dynamos with a particular focus on the MSC effect and our results suggest that it can likely operate in the differentially rotating and stably stratified plasma of a stellar RZ. The dynamo loop closed by the MSC effect (Rogachevskii & Kleeorin 2004; Squire & Bhattacharjee 2015c, a, 2016) generates toroidal field from the shearing of a poloidal field and regenerates poloidal field from the toroidal field through statistical correlations of local, non-helical MHD turbulence. Our analysis is based on idealized theory and simulations modeling a local section of an RZ, providing evidence to support a broader picture of dynamos in RZs. The key pieces of evidence are:

(i) Perturbative mean-field dynamo theory, when extended to include stable stratification (along the direction of shear), predicts the MSC instability remains robust with a decreased growth rate compared to the unstratified case. The hydrodynamic VD, however, is rapidly stabilized by stratification.

(ii) Shearing box simulations show that a mean shear combined with an unstable SSD in stably stratified turbulence is unstable to an LSD, qualitatively agreeing with mean-field dynamo theory. The simulations also confirm that the hydrodynamic VD is stabilized by the addition of weak stable stratification.

(iii) Simulations show that the energy in the mean (toroidal) magnetic field at saturation is comparable to the turbulent kinetic energy.

(iv) A numerical scan of the magnetic Reynolds number demonstrates that the LSD does not suffer catastrophic quenching. In particular, the saturation time and amplitude are found to be independent of Rm. This is expected because there are no obvious constraints arising from magnetic helicity conservation on a non-helical dynamo mechanism.

Put together, these idealized results suggest that the MSC effect in an RZ requires (1) a source of non-helical magnetic fluctuations and (2) sufficient radial DR (velocity shear). The resulting mean-field should saturate at near-equipartition with the magnetic fluctuations in a manner that is free from catastrophic quenching (a significant issue for helicity-based alpha dynamo mechanisms).

Extrapolating our results from a local shearing box model to a realistic RZ, we propose two pathways to provide non-helical magnetic fluctuations for operation of an LSD through the MSC effect in a region of radial DR. The first is Tayler instabilities (Tayler 1973; Markey & Tayler 1973) of the toroidal field, which directly result in the magnetic fluctuations that we propose may drive the MSC effect and regenerate axisymmetric poloidal field, thereby closing the Tayler–Spruit dynamo (Spruit 2002; Fuller et al. 2019). The second is the SSD operating in stably stratified turbulence, which may be driven by instabilities of latitudinal DR (Zahn 1974, 1992; Prat & Lignières 2013, 2014; Cope et al. 2020; Garaud 2020). The reality may be a mixture of the two processes, and perhaps others. Although significant uncertainties remain (effects of spherical geometry, the helicity fraction of instability-driven magnetic turbulence, low Prandtl numbers etc.), the near-equiparition saturation, robustness to stable stratification and immunity to catastrophic quenching of the

Downloaded from https://academic.oup.com/mnras/article/517/1/526/6711698 by Princeton University user on 30 August 2023

MSC effect make it worthy of further consideration in more complex global dynamo models in stellar RZs.

ACKNOWLEDGEMENTS

AB was supported by the DOE grant for the Max Planck Princeton Center (MPPC). JS was supported by a Rutherford Discovery Fellowship RDF-U001804, which is managed through the Royal Society Te Apārangi. VS was supported by Max-Planck/Princeton Center for Plasma Physics (NSF grant PHY-1804048). We thank Axel Brandenburg and members of the 'Magnetic Field Evolution in Low Density or Strongly Stratified Plasmas' conference for helpful discussions and Kailey Whitman for help with generation of the diagrams.

6 DATA AVAILABILITY

All numerical data was generated using the publicly available SNOOPY code (Lesur 2015). The data underlying this article will be shared on reasonable request to the corresponding author.

REFERENCES

Bartello P., Tobias S., 2013, J. Fluid Mech., 725, 1
Bhat P., Subramanian K., Brandenburg A., 2016, MNRAS, 461, 240
Bhattacharjee A., Yuan Y., 1995, ApJ, 449, 739
Billant P., Chomaz J.-M., 2001, Phys. Fluids, 13, 1645
Balogh A., Bykov A., Eastwood J., Kaastra J., 2016, Space Sciences Series of ISSI, Vol. 51, Multi-scale Structure Formation and Dynamics in Cosmic Plasmas. Springer, New York, NY
Blackman E. G., Chou T., 1997, ApJ, 489, L95
Blackman E. G., Field G. B., 2000, ApJ, 534, 984
Brandenburg A., 2001, ApJ, 550, 824
Brandenburg A., 2018, J. Plasma Phys., 84, 20
Brandenburg A., Subramanian K., 2005a, Astron. Nachr. Astron. Notes, 326, 400
Brandenburg A., Subramanian K., 2005b, Phys. Rep., 417, 1
Brandenburg A., Dobler W., Subramanian K., 2002, Astron. Nachr. Astron. Notes, 323, 99
Brandenburg A., Rädler K.-H., Rheinhardt M., Käpylä P., 2008, ApJ, 676, 740
Brethouwer G., Billant P., Lindborg E., Chomaz J.-M., 2007, J. Fluid Mech., 585, 343
Cantiello M., Mankovich C., Bildsten L., Christensen-Dalsgaard J., Paxton B., 2014, ApJ, 788, 93
Cattaneo F., Hughes D. W., 1996, Phys. Rev. E, 54, R4532
Chini G. P., Michel G., Julien K., Rocha C. B., Caulfield C.-c. P., 2022, J. Fluid Mech., 933, A22
Cope L., Garaud P., Caulfield C., 2020, J. Fluid Mech., 903, A1
Courvoisier A., Hughes D., Proctor M., 2010, Astron. Nachr., 331, 667
Den Hartogh J., Eggenberger P., Deheuvels S., 2020, A&A, 634, L16
Eggenberger P. et al., 2017, A&A, 599, A18
Eggenberger P., den Hartogh J., Buldgen G., Meynet G., Salmon S., Deheuvels S., 2019, A&A, 631, L6
Elperin T., Kleeorin N., Rogachevskii I., 2003, Physical Review E - Statistical Physics, Plasmas, Fluids, and Related Interdisciplinary Topics, 68, 8
Faucher-Giguere C.-A., Kaspi V. M., 2006, ApJ, 643, 332
Fuller J., Lu W., 2022, MNRAS, 511, 3951
Fuller J., Piro A. L., Jermyn A. S., 2019, MNRAS, 485, 3661
Garaud P., 2020, ApJ, 901, 146
Garaud P., 2021, Phys. Rev. Fluids, 6, 030501
Gruzinov A., Diamond P., 1994, Phys. Rev. Lett., 72, 1651
Gullón M., Miralles J. A., Viganò D., Pons J. A., 2014, MNRAS, 443, 1891
Heger A., Langer N., Woosley S., 2000, ApJ, 528, 368
Heinemann T., McWilliams J., Schekochihin A., 2011, Phys. Rev. Lett., 107, 255004
Hermes J. et al., 2017, ApJS, 232, 23
Hughes D. W., Rosner R., Weiss N. O., 2007, The Solar Tachocline. Cambridge Univ. Press
Iskakov A. B., Schekochihin A. A., Cowley S. C., McWilliams J. C., Proctor M. R. E., 2007, Phys. Rev. Lett., 98, 208501
Käpylä P. J., Mitra D., Brandenburg A., 2009, Physical Review E - Statistical, Nonlinear, and Soft Matter Physics, 79, 016302
Käpylä M. J., Rheinhardt M., Brandenburg A., 2022, ApJ, 932, 8
Kissin Y., Thompson C., 2018, ApJ, 862, 111
Kleeorin N., Moss D., Rogachevskii I., Sokoloff D., 2000, Astron. Astrophys, 361, L5
Kundu P. K., Cohen I. M., 2002, Fluid Mechanics. Academic Press, San Diego
Lesur G., 2015, available at: https://ipag.osug.fr/~lesurg/snoopy.html
Lesur G., Ogilvie G., 2008, A&A, 488, 451
Lindborg E., 2006, J. Fluid Mech., 550, 207
MacFadyen A., Woosley S., 1999, ApJ, 524, 262
Maffioli A., Davidson P. A., 2016, J. Fluid Mech., 786, 210
Markey P., Tayler R., 1973, MNRAS, 163, 77
Mitra D., Brandenburg A., 2012, MNRAS, 420, 2170
Ouazzani R.-M., Marques J., Goupil M.-J., Christophe S., Antoci V., Salmon S., Ballot J., 2019, A&A, 626, A121
Ozmidov R., 1992, J. Marine Syst., 3, 417
Prat V., Lignières F., 2013, A&A, 551, L3
Prat V., Lignières F., 2014, A&A, 566, A110
Rädler K.-H., Stepanov R., 2006, Phys. Rev. E, 73, 056311
Rheinhardt M., Brandenburg A., 2010, A&A, 520, A28
Riley J. J., Lelong M.-P., 2000, Ann. Rev. Fluid Mech., 32, 613
Riley J. J., Lindborg E., 2010, Ten Chapters in Turbulence. Cambridge Univ. Press, Cambridge, England, p. 269
Rincon F., 2019, J. Plasma Phys., 85, 205850401
Rincon F., 2021, Phys. Rev. Fluids, 6, L121701
Rogachevskii I., Kleeorin N., 2004, Phys. Rev. E, 70, 046310
Roulet J., Chia H. S., Olsen S., Dai L., Venumadhav T., Zackay B., Zaldarriaga M., 2021, Phys. Rev. D, 104, 083010
Shi J.-M., Stone J. M., Huang C. X., 2016, MNRAS, 456, 2273
Singh N. K., Sridhar S., 2011, Phys. Rev. E, 83, 056309
Skoutnev V. A., 2022, preprint (arXiv:2205.01540)
Skoutnev V., Squire J., Bhattacharjee A., 2021, ApJ, 906, 61
Spiegel E. A., Veronis G., 1960, ApJ, 131, 442
Spruit H., 2002, A&A, 381, 923
Squire J., Bhattacharjee A., 2015a, Phys. Rev. E, 92, 053101
Squire J., Bhattacharjee A., 2015b, Phys. Rev. Lett., 114, 085002
Squire J., Bhattacharjee A., 2015c, Phys. Rev. Lett., 115, 175003
Squire J., Bhattacharjee A., 2015d, ApJ, 813, 52
Squire J., Bhattacharjee A., 2016, J. Plasma Phys., 82, 535820201
Squire J., Burby J., Qin H., 2014, Comp. Phys. Commun., 185, 128
Tayler R., 1973, MNRAS, 161, 365
Teed R. J., Proctor M. R., 2016, MNRAS, 458, 2885
Vishniac E. T., Brandenburg A., 1997, ApJ, 475, 263
Vishniac E. T., Cho J., 2001, ApJ, 550, 752
Waite M. L., Bartello P., 2004, J. Fluid Mech., 517, 281
Wissing R., Shen S., Wadsley J., Quinn T., 2022, A&A, 659, A91
Yoon S.-C., Langer N., Norman C., 2006, A&A, 460, 199
Yousef T., Heinemann T., Schekochihin A., Kleeorin N., Rogachevskii I., Iskakov A., Cowley S., McWilliams J., 2008, Phys. Rev. Lett., 100, 184501
Zahn J.-P., 1974, Symposium-International Astronomical Union. Cambridge Univ. Press, Cambridge, England, p. 185
Zahn J.-P., 1992, Astron. Astrophys., 265, 115
Zahn J.-P., Brun A., Mathis S., 2007, A&A, 474, 145
Zaldarriaga M., Kushnir D., Kollmeier J. A., 2018, MNRAS, 473, 4174
Zeldovich I. B., Ruzmaikin A. A., 1980, Zhurnal Eksperimentalnoi i Teoreticheskoi Fiziki, 78, 980
Zhou H., Blackman E. G., 2021, MNRAS, 507, 5732
Zier O., Springel V., 2022, MNRAS, preprint (arXiv:2208.01065)

Downloaded from https://academic.oup.com/mnras/article/517/1/526/6711698 by Princeton University user on 30 August 2023

APPENDIX A: ELECTROMOTIVE FORCE CALCULATION FOR THE MHD BOUSSINESQ EQUATIONS

The general set-up for calculating mean field transport coefficients using the SOCA supposes a bath of homogeneous and isotropic velocity and magnetic field fluctuations in the presence of anisotropic perturbations such as shear flows $\boldsymbol{U}_0$ of form $U_i = U_{ij}x_j$ (with no vertical component $U_x = 0$ in the Boussinesq case), rotation (Ω), and stable stratification (in the $\hat{x}$ direction with Brunt–Vaisala frequency N). While rotation is not included in the main paper, it is simple to include it here to demonstrate the mean-field MHD Boussinesq framework for the full problem. We assume the mean velocity field does not evolve and write the total fields as $\boldsymbol{U}_T = \boldsymbol{U}_0 + \boldsymbol{u}$, $\boldsymbol{B}_T = \boldsymbol{B} + \boldsymbol{b}$, and $\Theta_T = \theta$ ($\Theta = 0$ because there cannot be any mean vertical flows that could drive Θ). The mean field induction equation then is given by

$$\partial_t \boldsymbol{B} = \nabla \times (\boldsymbol{U}_0 \times \boldsymbol{B}) + \nabla \times \mathcal{E} + \eta \nabla^2 \boldsymbol{B}, \tag{A1}$$

where the EMF is

$$\mathcal{E} = \langle \boldsymbol{u} \times \boldsymbol{b} \rangle = \mathcal{E}(\boldsymbol{B}). \tag{A2}$$

The fluctuation equations for $\boldsymbol{u}$, $\boldsymbol{b}$, and θ are obtained by subtracting the mean field equations from those of the total fields:

$$\partial_t \boldsymbol{u} + \boldsymbol{u} \cdot \nabla \boldsymbol{U}_0 + \boldsymbol{U}_0 \cdot \nabla \boldsymbol{u} + (\boldsymbol{u} \cdot \nabla \boldsymbol{u})' + 2\boldsymbol{\Omega} \times \boldsymbol{u} = -\nabla p + \theta \hat{x} + \boldsymbol{B} \cdot \nabla \boldsymbol{b} + \boldsymbol{b} \cdot \nabla \boldsymbol{B} + (\mathbf{b} \cdot \nabla \boldsymbol{b})' + \nu \nabla^2 \boldsymbol{u} + \sigma_f, \tag{A3}$$

$$\partial_t \boldsymbol{b} = \nabla \times (\boldsymbol{U}_0 \times \boldsymbol{b} + \boldsymbol{u} \times \boldsymbol{B} + (\boldsymbol{u} \times \boldsymbol{b})') + \eta \nabla^2 \boldsymbol{b}, \tag{A4}$$

$$\partial_t \theta + \boldsymbol{U}_0 \cdot \nabla \theta + (\boldsymbol{u} \cdot \nabla \theta)' = -N^2 u_x + \kappa \nabla^2 \theta, \tag{A5}$$

$$\nabla \cdot \boldsymbol{u} = 0, \ \nabla \cdot \boldsymbol{b} = 0, \tag{A6}$$

where we have used the notation $(A)' = A - \langle A \rangle$.

Following Rädler & Stepanov (2006), the EMF $\mathcal{E}$ can be Taylor expanded and linearly related to the mean field B_i and its derivative $B_{i,j}$ (i.e. $\mathcal{E}_i = a_{i,j}B_j + b_{ijk}B_{j,k}...$) assuming sufficient scale separation. This then provides a closure of the mean field induction equation. Taking into account all symmetry properties, the most general form of transport coefficients linearly relating $\mathcal{E}$ and $\boldsymbol{B}$ is

$$\begin{aligned}\mathcal{E} = &-\alpha_H^{(0)}\boldsymbol{B} - \alpha_H^{(D)} D_{ij} B_j - \gamma_H^{(\Omega)} \boldsymbol{\Omega} \times \boldsymbol{B} - \gamma_H^{(W)} \boldsymbol{W} \times \boldsymbol{B} \\ &- \alpha_1^{(\Omega)} (\hat{\boldsymbol{g}} \cdot \boldsymbol{\Omega}) \boldsymbol{B} - \alpha_2^{(\Omega)} [(\hat{\boldsymbol{g}} \cdot \boldsymbol{B}) \boldsymbol{\Omega} + (\boldsymbol{B} \cdot \boldsymbol{\Omega}) \hat{\boldsymbol{g}}] - \alpha_1^{(W)} (\boldsymbol{g} \cdot \boldsymbol{W}) \boldsymbol{B} \\ &- \alpha_2^{(W)} [(\hat{\boldsymbol{g}} \cdot B) \boldsymbol{W} + (\boldsymbol{B} \cdot \boldsymbol{W}) \hat{\boldsymbol{g}}] \\ &- \alpha^{(D)} (\epsilon_{ilm} D_{lj} \hat{g}_m + \epsilon_{jlm} D_{li} \hat{g}_m) B_j \\ &- (\boldsymbol{\gamma}^{(0)} + \gamma^{(\Omega)} \hat{\boldsymbol{g}} \times \boldsymbol{\Omega} + \gamma^{W} \hat{\boldsymbol{g}} \times \boldsymbol{W} + \gamma^{(D)} D_{ij} \hat{g}_j) \times \boldsymbol{B} \\ &- \beta^{(0)} \boldsymbol{J} - \beta^{(D)} D_{ij} J_j - (\delta^{(W)} \boldsymbol{W} + \delta^{(\Omega)} \boldsymbol{\Omega}) \times \boldsymbol{J} \\ &- (\kappa^{(W)} \boldsymbol{W} + \kappa^{\Omega} \boldsymbol{\Omega})_j (\nabla \boldsymbol{B})^{(s)}_{ji} - 2\kappa^{(D)} \epsilon_{ijk} D_{kr} (\nabla \boldsymbol{B})^{(s)}_{jr}.\end{aligned} \tag{A7}$$

The calculation of $\mathcal{E}$ at this point can be carried out with the help of the SOCA. The SOCA assumes that the higher order correlation terms (the primed terms such as $(\boldsymbol{u} \cdot \nabla \boldsymbol{u})'$) are small compared to terms involving the mean fields (e.g. $\boldsymbol{u} \cdot \nabla \boldsymbol{U}_0$) and can be neglected. This will lead to linear time evolution equations for $\boldsymbol{u}$, $\boldsymbol{b}$, and θ that can be solved perturbatively. The perturbation expansion is done on both $\mathbf{u}$ and $\mathbf{b}$ around their background, homogeneous fluctuation values $\boldsymbol{u}_0$ and $\boldsymbol{b}_0$ and then substituted into equation (A2) for the EMF. While statistics of the background fluctuations will be assumed, they physically arise from the forcing term σ_f of the momentum equation (sustaining $\boldsymbol{u}_0$) and a resulting small-scale dynamo (sustaining $\boldsymbol{b}_0$ in equipartition). The forcing itself models some hydrodynamic instability, such as horizontal shear instabilities discussed in the main article. In general, the background fluctuations have both helical and non-helical components, which we include in the calculation. To allow the perturbative expansion, all anisotropic parameters such as N^2, S, Ω are considered to be small. With the notation $\boldsymbol{u} = \boldsymbol{u}_0 + \boldsymbol{u}^{(0)} + \boldsymbol{u}^{(1)}...$ for the expansion of $\boldsymbol{u}$ (as well as $\boldsymbol{b}$ and θ), $\mathcal{E}$ to second order is

$$\begin{aligned}\mathcal{E} = &\langle \boldsymbol{u}_0 \times \boldsymbol{b}^{(0)} \rangle + \langle \mathbf{u}^{(0)} \times \boldsymbol{b}_0 \rangle + \langle \boldsymbol{u}^{(0)} \times \boldsymbol{b}^{(0)} \rangle \\ &+ \langle \boldsymbol{u}_0 \times \boldsymbol{b}^{(1)} \rangle + \langle \boldsymbol{u}^{(1)} \times \boldsymbol{b}_0 \rangle,\end{aligned} \tag{A8}$$

where $\langle \boldsymbol{u}_0 \times \boldsymbol{b}_0 \rangle = 0$ is assumed.

The calculation of $\mathcal{E}$ is carried out in Fourier space and explained in detail in Rädler & Stepanov (2006). We only give a brief description of the approach in order to point out how we handle the new addition of the buoyancy equation and the bouyancy term in the momentum equation in the SOCA formalism. To begin, we write out the evolution equations in real space for each order by applying the expansion to the fluctuation equations and then using the SOCA where applicable. The background, zeroth-order, and first-order equations are shown below.

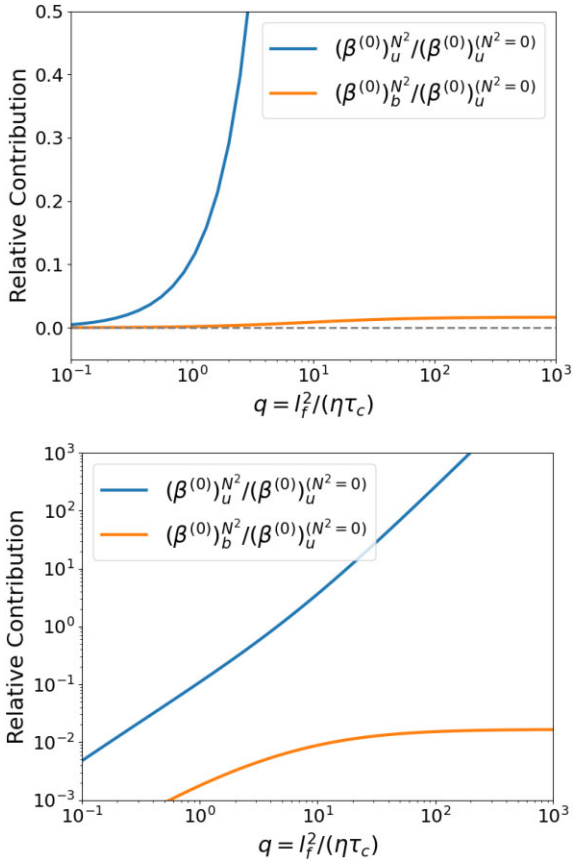

Figure A1. The modification of the isotropic turbulent resistivity by stratification. Plots of the ratio of the stratification term to the unstratified term on a linear (top) and a log scale (bottom). The contribution to the stratification term from velocity fluctuations is in blue and from magnetic fluctuations is in orange.

A1 Background turbulence

The homogeneous, background fluctuations satisfy

Downloaded from https://academic.oup.com/mnras/article/517/1/526/6711698 by Princeton University user on 30 August 2023

$$\partial_t \boldsymbol{u}_0 + (\boldsymbol{u}_0 \cdot \nabla \boldsymbol{u}_0)' = -\nabla p_0 + \theta_0 \hat{x} + (\boldsymbol{b}_0 \cdot \nabla \boldsymbol{b}_0)' + \nu \nabla^2 \boldsymbol{u}_0 + \sigma_f, \tag{A9}$$

$$\partial_t \boldsymbol{b}_0 = \nabla \times (\boldsymbol{u}_0 \times \boldsymbol{b}_0)' + \eta \nabla^2 \boldsymbol{b}_0, \tag{A10}$$

$$\partial_t \theta_0 + \boldsymbol{u}_0 \cdot \nabla \theta_0 = \kappa \nabla^2 \theta_0. \tag{A11}$$

While the homogeneous velocity and magnetic fluctuations $\boldsymbol{u}_0$ and $\boldsymbol{b}_0$ are assumed to be in a steady state driven by the forcing σ_f and a SSD, the buoyancy equation for the buoyancy fluctuations does not have any source term. Therefore, any initial buoyancy variable fluctuations $\theta_0(t = 0)$ will be passively advected and thermally diffuse to zero after a transient phase. These background equations themselves are not used in the calculation for $\mathcal{E}$, but a model for the homogeneous statistics of the background turbulence will be used.

A2 Zeroth order

The SOCA approximation assumes terms such as $(\boldsymbol{u}^{(0)} \cdot \nabla \boldsymbol{u}^{(0)})'$ are much smaller than $\boldsymbol{u}_0 \cdot \nabla \boldsymbol{U}_0$ so then the equations for the zeroth-order fluctuations become

$$(\partial_t - \nu \nabla^2)\boldsymbol{u}^{(0)} = -(\boldsymbol{U}_0 \cdot \nabla \boldsymbol{u}_0 + \boldsymbol{u}_0 \cdot \nabla \boldsymbol{U}_0) - \nabla p^{(0)} - 2\boldsymbol{\Omega} \times \boldsymbol{u}_0 + \theta^{(0)} \hat{x} + \boldsymbol{B} \cdot \nabla \boldsymbol{b}_0 + \boldsymbol{b}_0 \cdot \nabla \boldsymbol{B}, \tag{A12}$$

$$(\partial_t - \eta \nabla^2)\boldsymbol{b}^{(0)} = \nabla \times (\boldsymbol{U}_0 \times \mathbf{b}_0 + \boldsymbol{u}_0 \times \boldsymbol{B}), \tag{A13}$$

$$(\partial_t - \kappa \nabla^2)\theta^{(0)} = -N^2 u_{0,x}, \tag{A14}$$

where we have dropped the $\boldsymbol{U}_0 \cdot \nabla \theta_0$ term in the buoyancy equation (A14) because the θ_0 fluctuations are zero after a transient phase as discussed above.

A3 First order

Similarly, the equations for the first-order fluctuations are as follows:

$$(\partial_t - \nu \nabla^2)\boldsymbol{u}^{(1)} = -(\boldsymbol{U}_0 \cdot \nabla \boldsymbol{u}^{(0)} + \boldsymbol{u}^{(0)} \cdot \nabla \boldsymbol{U}_0) - \nabla p^{(1)} - 2\boldsymbol{\Omega} \times \boldsymbol{u}^{(0)} + \theta^{(1)} \hat{x} + \boldsymbol{B} \cdot \nabla \boldsymbol{b}^{(0)} + \boldsymbol{b}^{(0)} \cdot \nabla \boldsymbol{B}, \tag{A15}$$

$$(\partial_t - \eta \nabla^2)\boldsymbol{b}^{(1)} = \nabla \times (\boldsymbol{U}_0 \times \boldsymbol{b}^{(0)} + \boldsymbol{u}^{(0)} \times \boldsymbol{B}), \tag{A16}$$

$$(\partial_t - \kappa \nabla^2)\theta^{(1)} = -\boldsymbol{U}_0 \cdot \nabla \theta^{(0)} - N^2 u_x^{(0)}. \tag{A17}$$

A4 Calculation of $\mathcal{E}$

The calculation of $\mathcal{E}$ proceeds exactly as in Squire & Bhattacharjee (2015a) except with the addition of the buoyancy terms. The zeroth- and first-order fluctuation equations (A12) through (A17) are transformed to Fourier space and substituted into the Fourier space version of EMF equation (A8) [see Squire & Bhattacharjee (2015a) and Rädler & Stepanov (2006) for extensive details]. Because θ_0 fluctuations diffuse away and are not relevant for the background turbulence, it is unnecessary to make an additional model of the turbulent statistics between θ_0 and either $\boldsymbol{u}_0$ or $\boldsymbol{b}_0$. The lack of θ_0 is what allows $\theta^{(0)}$ and $\theta^{(1)}$ to be solved for in terms of $\boldsymbol{u}_0$ and $\boldsymbol{u}^{(0)}$ using the buoyancy equations (A14) and A17 and then substituted directly into the momentum equations (A12) and (A15), respectively. The net result of weak stably stratification therefore is added terms proportional to N^2 in the momentum equations (A12) and (A15).

We use the open source VEST package (Squire, Burby & Qin 2014) for Mathematica to carry out the calculation, similar to Squire & Bhattacharjee (2015a), including both helical and non-helical portions of the background velocity and magnetic fluctuations. We report only the four transport coefficients that we find are modified by stable stratification, the isotropic turbulent resistivity and alpha coefficient. All other transport coefficients are identical to the result in Squire & Bhattacharjee (2015a). The modified coefficients in Fourier space are shown below:

$$(\tilde{\beta}^{(0)})_u = \frac{u_{\rm rms} l_f}{\eta}\left[\frac{\tilde{k}^2}{3(\tilde{k}^4 + q^2\tilde{\omega}^2)} + \frac{3(N\tau_c)^2\tilde{k}^2(\tilde{k}^2\frac{Pm^2}{Pr} - q^2\tilde{\omega}^2)}{10(\tilde{k}^4 + q^2\tilde{\omega}^2)(\tilde{k}^4 Pm^2 + q^2\tilde{\omega}^2)(\tilde{k}^4\frac{Pm^2}{Pr^2} + q^2\tilde{\omega}^2)}\right], \tag{A18}$$

$$(\tilde{\beta}^{(0)})_b = (N\tau_c)^2\left[\frac{q^2\tilde{k}^2(\tilde{k}^4\frac{Pm^3}{Pr^2} - (\frac{Pm}{Pr} + 2Pm)q^2\tilde{\omega}^2)}{60(\tilde{k}^4 Pm^2 + q^2\tilde{\omega}^2)^2(\tilde{k}^4\frac{Pm^2}{Pr^2} + q^2\tilde{\omega}^2)}\right], \tag{A19}$$

$$(\tilde{\alpha}_H^{(0)})_u = \frac{u_{\rm rms} l_f}{\eta}\left[\frac{2\tilde{k}^2}{3(\tilde{k}^4 + q^2\tilde{\omega}^2)} + \frac{8(N\tau_c)^2\tilde{k}^2(\tilde{k}^2\frac{Pm^2}{Pr} - q^2\tilde{\omega}^2)}{15(\tilde{k}^4 + q^2\tilde{\omega}^2)(\tilde{k}^4 Pm^2 + q^2\tilde{\omega}^2)(\tilde{k}^4\frac{Pm^2}{Pr^2} + q^2\tilde{\omega}^2)}\right], \tag{A20}$$

$$(\tilde{\alpha}_H^{(0)})_b = \frac{u_{\rm rms} l_f}{\eta}\left[-\frac{2\tilde{k}^2 Pm}{3(\tilde{k}^4 Pm^2 + q^2\tilde{\omega}^2)} + (N\tau_c)^2\frac{4q^2\tilde{k}^2(\tilde{k}^4\frac{Pm^3}{Pr^2} - (\frac{Pm}{Pr} + 2Pm)q^2\tilde{\omega}^2)}{15(\tilde{k}^4 Pm^2 + q^2\tilde{\omega}^2)^2(\tilde{k}^4\frac{Pm^2}{Pr^2} + q^2\tilde{\omega}^2)}\right], \tag{A21}$$

where $\tilde{k} = k l_f$, $\tilde{\omega} = \omega\tau_c$, $q = l_f^2/\eta\tau_c$ is the ratio of the resistive to the correlation time (a measure conductivity), and τ_c and l_f are the turbulence correlation time and length. We note that $(N\tau_c)^2$ is assumed small in the perturbative approach of the SOCA. The formal bound requires that the stratification term be smaller than the dominant terms in the momentum equation, which can be clearly seen by considering the zeroth-order momentum and buoyancy equations and balancing the $\partial_t u_{0,x}^{(0)} \sim \theta^{(0)}$ and $\partial_t \theta^{(0)} \sim -N^2 u_{0,x}$ terms to get $|u_x^{(1)}| \sim (N\tau_c)^2|u_{0,x}|$. Therefore, $(N\tau_c)^2$ needs to be on the order of the perturbation expansion parameter.

The physical transport coefficients are obtained by an inverse Fourier transform given by $\beta^{(0)} = (\beta^{(0)})_u + (\beta^{(0)})_b = 4\pi \int d\tilde{k} d\tilde{\omega} \tilde{k}^2[(\tilde{\beta}^{(0)})_u W_u(\tilde{k}, \tilde{\omega}) + (\tilde{\beta}^{(0)})_b W_b(\tilde{k}, \tilde{\omega})]$, where W_u and W_b are the statistics of the non-helical background velocity and magnetic fluctuations, respectively. The non-helical velocity and magnetic fields are assumed to follow Gaussian statistics: $W_u(\tilde{k}, \tilde{\omega}) = W_b(\tilde{k}, \tilde{\omega}) = \frac{2\tilde{k}^2}{3(2\pi)^{5/2}} \exp(-\tilde{k}^2/2)/(1 + \tilde{\omega}^2)$ (Rädler & Stepanov 2006). The same applies for $\alpha_H^{(0)}$ but using the model statistics for the helical fraction of the turbulence. The isotropic turbulent resistivity here is the same as in the main article ($\eta_t = \beta^{(0)}$) but with a different notation. We are interested in quantifying the relative size of the stratification term to the unstratified value of $\beta^{(0)}$ since this term affects the MSC effect. To this end, we split the unstratified and stratified contributions to $\beta^{(0)}$ and then examine their ratio. For concreteness, we set unity Prandtl numbers (Pm = Pr = 1) and define the separate contributions as follows:

$$(\beta^{(0)})_u = (\beta^{(0)})_u^{(N^2=0)}(q) + (N\tau_c)^2(\beta^{(0)})_u^{N^2}(q), \tag{A22}$$

$$(\beta^{(0)})_b = (N\tau_c)^2(\beta^{(0)})_b^{N^2}(q), \tag{A23}$$

Downloaded from https://academic.oup.com/mnras/article/517/1/526/6711698 by Princeton University user on 30 August 2023

$$(\beta^{(0)})_u^{(N^2=0)}(q) = 4\pi \int \mathrm{d}\tilde{k}\mathrm{d}\tilde{\omega}\tilde{k}^2 \frac{\tilde{k}^2}{3(\tilde{k}^4+q^2\tilde{\omega}^2)}\tilde{W}_u(\tilde{k},\tilde{\omega}), \quad \text{(A24)}$$

$$(\beta^{(0)})_u^{N^2}(q) = 4\pi \int \mathrm{d}\tilde{k}\mathrm{d}\tilde{\omega}\tilde{k}^2 \frac{3q^2\tilde{k}^2(\tilde{k}^4-q^2\tilde{\omega}^2)}{10(\tilde{k}^4+q^2\tilde{\omega}^2)^3}\tilde{W}_u(\tilde{k},\tilde{\omega}), \quad \text{(A25)}$$

$$(\beta^{(0)})_b^{N^2}(q) = 4\pi \int \mathrm{d}\tilde{k}\mathrm{d}\tilde{\omega}\tilde{k}^2 \frac{q^2\tilde{k}^2(\tilde{k}^4-3q^2\tilde{\omega}^2)}{60(\tilde{k}^4+q^2\tilde{\omega}^2)^3}\tilde{W}_b(\tilde{k},\tilde{\omega}). \quad \text{(A26)}$$

Fig. A1 shows the relative size of $(\beta^{(0)})_u^{N^2}(q)$ and $(\beta^{(0)})_b^{N^2}(q)$ with respect to the unstratified value $(\beta^{(0)})_u^{(N^2=0)}(q)$ by plotting their ratios versus q, which can be thought of as a measure of the conductivity $q = \mathrm{Rm/St}$. Both kinetic and magnetic contributions from stratification are positive, which is expected since stratification should intuitively reduce the dynamo efficiency. We see that the kinetic contribution is much larger than the magnetic contribution $(\beta^{(0)})_b^{N^2}(q) \gg (\beta^{(0)})_u^{N^2}(q)$. As $q \to \infty$, the magnetic contribution remains small $\beta^{(0)})_b^{(N^2)}/(\beta^{(0)})_u^{(N^2=0)} \ll 1$. The kinetic contribution may become important as $q \to \infty$, since $(\beta^{(0)})_b^{N^2}(q)/(\beta^{(0)})_u^{(N^2=0)} \gg 1$ may become important. However, the formally valid limit $(N\tau_c)^2 \ll 1$ means that the contributions from stratification are still small compared to the unstratified isotropic turbulent resistivity. While $q \gg 1$ seems like the relevant limit for large Rm, recall that SOCA is only formally valid for $\mathrm{Rm} \ll 1$ at $q \ll 1$ or $\mathrm{St} \ll 1$ at $q \gg 1$. In reality, $q = O(1)$ probably provides the most reasonable estimate for non-linear turbulence (see discussions in Brandenburg & Subramanian 2005b; Rädler & Stepanov 2006; Squire & Bhattacharjee 2015a).

APPENDIX B: HELICITY GENERATION AND CATASTROPHIC QUENCHING

In this section, we first apply the two-scale approach to the total magnetic helicity, then describe how catastrophic quenching results from helicity constraints, and finally show that the MSC effect does not produce helicity. The resulting takeaway is that the MSC effect is immune to catastrophic quenching and therefore likely remains a robust mechanism in the astrophysical limit of large *Rm*.

The total magnetic helicity is given by $\mathcal{H}_T = \int \boldsymbol{A}_T \cdot \boldsymbol{B}_T \mathrm{d}V$, where $\boldsymbol{A}_T$ is the vector potential ($\boldsymbol{B}_T = \nabla \times \boldsymbol{A}_T$). $\mathcal{H}$ can be split into the helicity of the large scale and small-scale magnetic fields $\mathcal{H} = \int \mathbf{A} \cdot \mathbf{B} dV$ and $h = \int \langle \boldsymbol{a} \cdot \boldsymbol{b} \rangle \mathrm{d}V$, where brackets denote the mean field average. Using $\partial_t \boldsymbol{A}_T = -\boldsymbol{E}_T + \nabla\phi$ from the induction equation (where $\boldsymbol{E}_T = \boldsymbol{U}_T \times \boldsymbol{B}_T + \eta\nabla \times \boldsymbol{B}_T$ is the electric field and ϕ is an arbitrary scalar field), it is straightforward to show that

$$\partial_t \mathcal{H} = +2\int \mathcal{E} \cdot \boldsymbol{B}\mathrm{d}V - 2\eta \int (\nabla \times \boldsymbol{B}) \cdot \boldsymbol{B}\mathrm{d}V, \quad \text{(B1)}$$

$$\partial_t h = -2\int \mathcal{E} \cdot \boldsymbol{B}\mathrm{d}V - 2\eta \int \langle(\nabla \times \boldsymbol{b}) \cdot \boldsymbol{b}\rangle \mathrm{d}V, \quad \text{(B2)}$$

where we have assumed helicity fluxes through the volume boundaries are zero due to periodicity or perfectly conducting boundary conditions. The argument for quenching of helical dynamos stems from the observation that large scale and small scale helicities are produced through the EMF at the same rate, but with opposite signs (Rincon 2019) (i.e. the source term is $\pm 2\int \mathcal{E} \cdot \boldsymbol{B}\mathrm{d}V$). Consider a turbulent MHD system at large *Rm* with a growing, but still weak mean magnetic field. The SSD will be the first to saturate and so the small-scale helicity will remain roughly constant $\partial_t h \approx 0$, leaving a balance between between helicity injection and dissipation at small scales in equation (B2) (i.e. $2\int \mathcal{E} \cdot \boldsymbol{B} dV \approx -2\eta \int \langle(\nabla \times \boldsymbol{b}) \cdot \boldsymbol{b}\rangle \mathrm{d}V$). As a result, the large-scale helicity in equation (B1) becomes constrained to grow at the dissipation rate of small-scale helicity, $\partial_t H \approx -2\eta \int \langle(\nabla \times \boldsymbol{b}) \cdot \boldsymbol{b}\rangle \mathrm{d}V$ (since dissipation of helicity by the small-scale fields is much faster than by the large-scale fields). The dependence of $\partial_t \mathcal{H}$ on the microscopic resistivity η leads to a resistivity limited growth (catastrophic quenching) of the large-scale dynamo in the astrophysical limit of $\eta \to 0$ (i.e. $\mathrm{Rm} \to \infty$). It may be possible to avoid catastrophic quenching if small-scale helicity can be transported out of the domain boundaries at the production rate of large-scale helicity by dropping the ideal boundary condition assumption. However, simulations have so far found mixed results (Rincon 2019).

LSDs driven by helical turbulence produce helical large-scale fields because the form of the EMF gives a non-zero source term. For example, the simplest alpha dynamo $\mathcal{E}_i = \alpha_H^{(0)} \boldsymbol{B}_i$ has $\int \mathcal{E} \cdot \boldsymbol{B}\mathrm{d}V = \alpha_H^{(0)} \int |\boldsymbol{B}|^2 \mathrm{d}V \neq 0$ and $\partial_t \mathcal{H} \neq 0$. The same can be shown for all other alpha-effect based dynamos (e.g. α–Ω dynamos) whose transport coefficients (such as $\alpha_H^{(0)}$, $\alpha_H^{(D)}$, etc.) are based on the helical part of the background turbulence.

On the other hand, LSDs driven by non-helical turbulence generate non-helical large scale fields because the source term is zero. The MSC effect is an example of the general class of shear-current effects that have contributions from the following terms in the EMF:

$$\mathcal{E}_i^{\mathrm{SC}} = -\beta^{(D)} D_{ij} \boldsymbol{J}_j - \delta^{(W)} \epsilon_{ijk} W_j \boldsymbol{J}_k - \kappa^{(W)} W_j (\nabla \boldsymbol{B})_{ji}^{(s)} - 2\kappa^{(D)} \epsilon_{ijk} D_{kr} (\nabla \boldsymbol{B})_{jr}^{(s)}. \quad \text{(B3)}$$

The crucial coefficient in the MSC effect, $\eta_{yx} = -\delta^{(W)} + \frac{1}{2}(\kappa^{(W)} - \beta^{(D)} + \kappa^{(D)})$, has contributions from each of these terms. It is straightforward to show that $\int \mathcal{E}^{\mathrm{SC}} \cdot \boldsymbol{B}\mathrm{d}V = 0$, with each term independently having a null contribution. Consider the term proportional to $\kappa^{(W)}$:

$$\int \kappa^{(W)} W_j (\nabla \boldsymbol{B})_{ji}^{(s)} B_i \mathrm{d}V = \frac{1}{2}\kappa^{(W)} W_j \int \left(\frac{\partial \boldsymbol{B}_j}{\partial x_i} + \frac{\partial \boldsymbol{B}_i}{\partial x_j} \right) \times B_i \mathrm{d}V = \quad \text{(B4)}$$

$$= \frac{1}{2}\kappa^{(W)} W_j \int \left(\frac{\partial (B_j B_i)}{\partial x_i} + \frac{\partial (B_i B_i)}{\partial x_j} \right) \times \mathrm{d}V = 0, \quad \text{(B5)}$$

where the divergence free condition has been used, $\frac{\partial B_i}{\partial x_i} = 0$, and we have assumed either periodic boundary conditions or that fields vanish sufficiently fast outside a finite region. Closed boundary conditions could in principle have a non-zero contribution (Brandenburg & Subramanian 2005a). The calculation for every other term is similar. As a result, the MSC effect, driven by non-helical magnetic fluctuations, generates non-helical large-scale magnetic fields and is not affected by the helicity constraints usually used to argue for the inevitability of catastrophic quenching at high *Rm*.

APPENDIX C: LONG TERM BEHAVIOR OF THE SATURATED LSD

This section briefly shows the dependence of the long term evolution of the saturated LSD on the domain size. Viewing the dynamo as an instability, fluctuations of the large scale magnetic field at the end of the rapid SSD phase will grow at rates given by the dispersion relation of any present LSD instabilities, which in this setup is a possible combination of the coherent MSC effect and incoherent effects. As discussed in Section 3.4, the incoherent effects become less efficient with increasing volume while coherent effects are volume independent (if the dominant mode fits in the domain). Fig. C1 compares the evolution of the saturated LSD across a long time scale $t/\tau_c = 3000$ (compared to the measured growth period

Downloaded from https://academic.oup.com/mnras/article/517/1/526/6711698 by Princeton University user on 30 August 2023

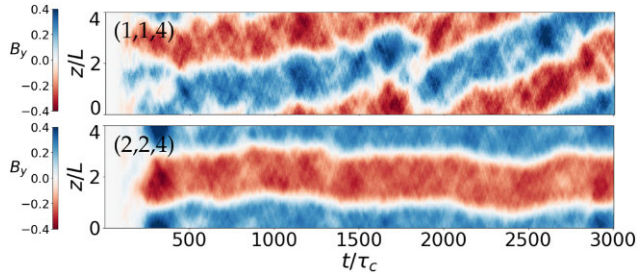

Figure C1. A test showing that the long-term trend of the saturated LSD phase becomes more coherent with increasing domain size where incoherent effects become less efficient. Time–space plots from single realizations of the y-component of the magnetic field $B_y(z, t) = \langle B_y(x, y, z, t)\rangle_{x,y}$ for two aspect ratios denoted in the top left corner of each plot are shown. Both simulations have fixed values of Rm $\approx$ 60, Sh $\approx$ 1.0, and $\mathrm{Fr}^{-1} \approx 0.2$ and the spectral resolution is scaled with the aspect ratio. The fiducial (1, 1, 4) simulation has $N_x \times N_y \times N_z = 96^2 \times 384$ modes.

of the LSD, $\gamma_{\mathrm{LSD}}^{-1} \sim 20\tau_c$ from Table 1) between the two cases with domain sizes (1, 1, 4) and (2, 2, 4). The (4, 4, 4) case is not included because it was too expensive to run for long times.

The long term evolution of the (1, 1, 4) case shown in the top panel of Fig. C1 has a constant phase for the first $t/\tau_c \sim 1000$ but then begins to very slowly vary on $t/\tau_c \sim 500$ time-scales. This may be related to the non-linear saturation mechanism of the MSC effect, an incoherent effect, or an interaction of the two. When the volume is quadrupled in the (2, 2, 4) case, any incoherent effect is expected to become suppressed by a factor of 2. As shown in the bottom panel of Fig. C1, the (2, 2, 4) case maintains a relatively steady phase across the entire duration as might be expected from the saturation of the coherent MSC effect alone (whose growth rate is purely real). This suggests that the domain volume is now sufficiently large that incoherent effects have become insignificant.

This paper has been typeset from a TEX/LATEX file prepared by the author.

Downloaded from https://academic.oup.com/mnras/article/517/1/526/6711698 by Princeton University user on 30 August 2023